

---

# TOWARDS MODEL PREDICTIVE CONTROL FOR SUPERCRITICAL CO<sub>2</sub> CYCLES

---

A PREPRINT

✉ **Viv A. Bone**

School of Mechanical and Mining Engineering  
The University of Queensland  
St Lucia, QLD, 4072  
v.bone@uq.edu.au

**Michael P. Kearney**

School of Mechanical and Mining Engineering  
The University of Queensland  
St Lucia, QLD, 4072  
m.kearney@uq.edu.au

✉ **Ingo H. J. Jahn**

School of Mechanical and Mining Engineering  
The University of Queensland  
St Lucia, QLD, 4072  
i.jahn@uq.edu.au

August 30, 2021

## ABSTRACT

Key challenges that complicate control of non-condensing non-ideal-gas power cycles include (1) their output power dynamics depend on interactions between turbomachinery and heat transfer processes, (2) turbomachinery behaviour cannot be captured by simple analytical relations, and (3) state constraints must be respected. This article presents a control methodology for these systems, comprising a control modelling approach and model predictive control (MPC) strategy. We demonstrate this methodology on the high-pressure side of a simple supercritical CO<sub>2</sub> cycle power block, composed of a variable-speed compressor, heat exchanger, and fixed-speed turbine. We develop a control model by using timescale-separation arguments and locally linearizing non-ideal-gas turbomachinery performance maps. We implement MPC by linearizing this control model online at each sampling instant. Closed-loop simulations with a full-order gas-dynamics truth model demonstrate the effectiveness of the proposed control methodology. In response to load changes, the controller maintains high turbine inlet temperatures while achieving net power output ramp rates in excess of 100% of nameplate output per minute. The controller often acts at the intersection of motor torque, compressor surge, and turbine inlet temperature constraints, and performs well from 35 to 105% of nameplate capacity with no parameter scheduling. The controller achieves good performance and fast update rates when using online linearization. The results demonstrate the suitability of MPC for the supercritical CO<sub>2</sub> cycle, and the proposed methodology is extensible to more complex cycle variants such as the recuperated and recompression cycle.

## 1 Introduction

A critical attribute of thermal power plants is their ‘flexibility’, which is their ability to operate over a wide range of power outputs and quickly change from one operating state to another, either by ramping or switching on or off. Flexibility has four main components: operating range, part-load efficiency, response times to load changes (i. e. ramp rate), and startup and shutdown times and costs [Feldmüller, 2018, ire, 2019]. Flexible power plants play a crucial role in maintaining grid reliability under demand- and supply-side variability [Kassakian et al., 2011], and they will become even more important as increasing renewable penetration further increases supply-side variability and uncertainty [ire, 2019, Duggal et al., 2017, , IEA]. Measures of flexibility like minimum load or maximum ramp rate are considered core performance metrics for modern power plants [VGB PowerTech e.V., 2017, Energiewende, 2017].

An impactful way to improve thermal power plant flexibility is to upgrade plant-level control systems [Duggal et al., 2017, VGB PowerTech e.V., 2017, Energiewende, 2017]. Advanced control systems can better coordinate plant subsystems during transients and facilitate operation closer to component design limits. These benefits enable operation at higher turn-downs, faster ramping, shorter and more reproducible start-ups and shut-downs, and decreased maintenance [ire, 2019, Duggal et al., 2017, Energiewende, 2017]. Some examples highlighting the importance of control are as follows: (1) installation of a new digital control system reduced the minimum load of a 600 MW lignite-fired plant by 27% [Energiewende, 2017]; (2) for steam plants, control schemes with dynamic wall models have permitted safe operation closer to thermal stress limits, thus increasing flexibility without increasing maintenance [VGB PowerTech e.V., 2017]; and (3) commissioning control loops over a wide operating range, rather than only at nominal load, has significantly improved part-load performance and ramp rates of coal-fired plants [VGB PowerTech e.V., 2017].

Control of thermal power plants, especially in dynamic load-following scenarios, is challenging for two key reasons: (1) power plants are multivariable nonlinear systems [Prasad et al., 1998, 2000, Kim et al., 2013, D’Amato et al., 2012, Yebi et al., 2017, Liu et al., 2017]; (2) power plants are subject to many constraints such as thermal stress limits [VGB PowerTech e.V., 2017], compressor surge [Gravdahl and Egeland, 2012], and turbomachinery blade loading limits [Kumar et al., 2012]. Given these challenges, a suitable control paradigm for this application is model predictive control (MPC), which performs well for multivariable systems, systematically handles constraints and plant nonlinearity, and provides a unified approach to control of complex systems [Maciejowski, 2002].

MPC involves periodically solving forward-looking constrained optimization problems to compute the control inputs that make a model of the plant best satisfy the control objectives while respecting all constraints [Maciejowski, 2002]. Only the first set of inputs is applied, then at the next sampling instant, the optimization problem is solved again to compute the subsequent set of inputs, and so on. The performance of MPC depends strongly on the accuracy and complexity of the model used by the controller, with more accurate models giving better calibrated control actions, and simpler models permitting faster updates or longer prediction horizons.

Existing literature confirms the value of MPC for established types of thermal power plants, such as steam Rankine cycle plants [Prasad et al., 1998, 2000], open- and closed-cycle gas turbines [Kim et al., 2013, Aurora et al., 2005, D’Amato, 2006, D’Amato et al., 2012], and organic Rankine cycle waste heat recovery units [Yebi et al., 2017, Liu et al., 2017, Rathod et al., 2019]. However, MPC has not yet been investigated for a key next-generation power cycle: the supercritical carbon dioxide (CO<sub>2</sub>) Brayton cycle (the ‘sCO<sub>2</sub> cycle’). This power cycle exploits CO<sub>2</sub>’s non-ideal-gas behavior to obtain higher thermal efficiencies than competing power cycles at readily-achieved turbine inlet temperatures (600–700 °C) [Musgrove and Wright, 2017]. The sCO<sub>2</sub> cycle is compact and scalable, being suitable for 10 MW rural plants up to multi-100 MW utility plants [Musgrove and Wright, 2017]. Additionally, due to the single-phase flow in the heater, the cycle can be well matched to many heat sources, and CO<sub>2</sub>’s moderate critical temperature makes the cycle compatible with non-polluting dry cooling systems [Turchi et al., 2013].

However, CO<sub>2</sub>’s non-ideal-gas behavior gives rise to complex cycle dynamics [Carstens, 2007, Moisseytsev and Sienicki, 2007], making the application of MPC to sCO<sub>2</sub> cycles particularly challenging. Critically, CO<sub>2</sub>’s strong property variations over the cycle’s operating range complicate modelling of heat exchangers and turbomachinery [Dostal, 2004, Carstens, 2007, Moisseytsev and Sienicki, 2007]. Additionally, most proposed sCO<sub>2</sub> cycles use non-condensing designs [Turchi et al., 2013, Rochau, 2011], so their mass flow and pressure dynamics (which strongly influence power output) arise from complex system interactions. Simulation models capture these dynamics implicitly using quasi-1D compressible flow solvers [Moisseytsev and Sienicki, 2007], but these models run slower than real time and are thus unsuitable for MPC. Existing control models for similar systems (such as air Brayton cycles) employ ideal-gas assumptions [Kim et al., 2013] and thus cannot be used for the sCO<sub>2</sub> cycle. It is currently unclear how to develop an explicit low-order model of sCO<sub>2</sub> cycle dynamics that is suitable for MPC.

This article proposes a control model that can be used to implement MPC for the high-pressure side of the sCO<sub>2</sub> cycle. The heat exchangers (and other fluid volumes) are modeled using a reduced-order gas-dynamics model [Bone et al., 2019], and the turbomachinery are modeled using performance maps with analytical off-design scaling [Jahn and Keep, 2017]. By considering the slow-timescale behavior of the system and linearizing the turbomachinery maps online, we derive an explicit low-order model for the slow-timescale evolution of mass flow, pressure, and net output power. This model can be fitted to individual plants by using modest experimental datasets to construct turbomachinery performance maps [Glassman, 1972] and tune heat exchanger models [Bone et al., 2018]. As the model is based primarily on first principles, it is somewhat robust to large extrapolation or overfitting errors, which may give rise to dangerous closed-loop behavior. This model is extensible to commercially-feasible sCO<sub>2</sub> cycle configurations such as the recuperated cycle and recompression cycle.

By linearizing the control model online, we implement MPC for the high-pressure side of a laboratory-scale open sCO<sub>2</sub> cycle, comprising a variable-speed compressor, printed circuit heat exchanger, fixed-speed turbine, and thermal oil heat input loop. The controller’s objective is to track net output power setpoints by manipulating compressor torque

and thermal oil flow rate, while also maximizing turbine inlet temperature and thus cycle thermodynamic efficiency. The controller must respect the compressor surge constraint and maximum wall temperature limits. To assess the performance of the proposed control scheme, we perform closed-loop simulations with a high-fidelity truth model that is calibrated to experimental heat exchanger, compressor, and turbine datasets. This truth model solves the full compressible flow equations and is essentially a quasi-1D computational fluid dynamics model. These simulations show the effectiveness of the proposed controller for the test system, suggesting that the proposed modelling and control strategies are valid. The results demonstrate MPC’s core strengths, namely constraint management, good dynamic performance for complex multivariable systems, and performance over a wide nonlinear operating range.

This article is organized as follows: Sec. 2 defines the control problem considered in this article; Sec. 3 presents the simulation model, including the fluid stream model, heat exchanger model, and the turbomachinery models; Sec. 3 discusses the derivation of a reduced-order control model from the simulation model and details how the constraints are modeled; Sec. 5 discusses the proposed control strategy; Sec. 6 presents the results of closed-loop simulations; and Sec. 7 concludes the article.

## 2 Control problem

This article presents an MPC scheme for the laboratory-scale open sCO<sub>2</sub> cycle shown in Fig. 1. This system comprises a centrifugal compressor, printed circuit heat exchanger (PCHE), radial inflow turbine, pump, and connecting pipework. The process stream working fluid is supercritical CO<sub>2</sub>, and the heat transfer fluid is Paratherm™ HE [par]. The compressor and turbine are on separate shafts. The compressor is asynchronous and is driven by an electric motor with controllable torque  $T_m$ , and the turbine is connected to the grid via a gear box operating at a synchronous speed of 1200 RPM. A pump drives mass flow in the thermal oil stream. We assume that a local proportional-integral-derivative (PID) controller manipulates pump speed to track the thermal oil mass flow rate setpoint  $\dot{m}_{oil,ref}$  (the dynamics of this local closed-loop system are given in Sec. 3.5). The MPC updates the setpoint of this local PID controller at each sampling instant.

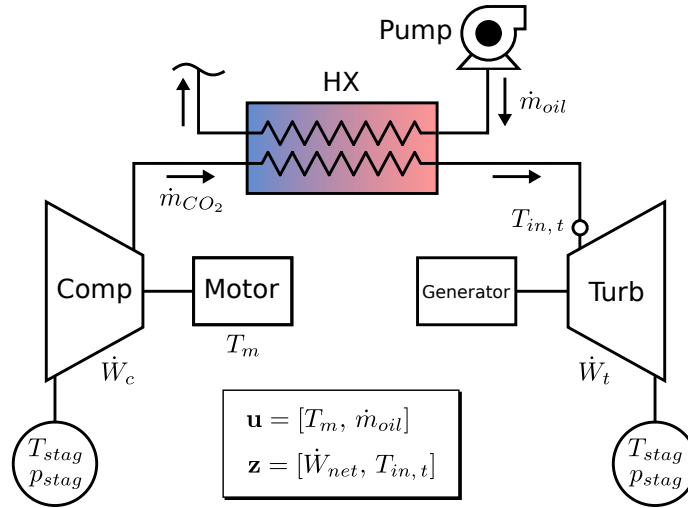


Figure 1: Open-cycle system showing inputs  $\mathbf{u}$  and tracked outputs  $\mathbf{z}$

The system parameter values are given in Tab. 1. These parameter values give a nominal power output of 65 kW, which is representative of a laboratory-scale sCO<sub>2</sub> cycle, rather than an efficient commercial facility. All pipes are assumed to be the same length. The cell counts  $N_{cells}$  refer to the discretization level of the components in the finite-volume flow solver (see Sec. 3). The compressor rotational inertia represents the compressor rotor plus the gearbox and motor. A sample set of steady-state operating conditions, corresponding to a power output of 55 kW and heat input of approximately 3100 kW, are shown in Fig. 2.

The objective of the control scheme presented in this article is regulate the turbine’s power output  $\dot{W}_t$  to some setpoint  $\dot{W}_{t,ref}$  while also driving the turbine inlet temperature to the target value  $T_{in,t,ref}$ . To maximize the system’s thermodynamic cycle efficiency,  $T_{in,t,ref}$  is set as the maximum feasible turbine inlet temperature that can be achieved for  $\dot{W}_{t,ref}$ . The control inputs are  $\dot{m}_{oil,ref}$  and  $T_m$ .

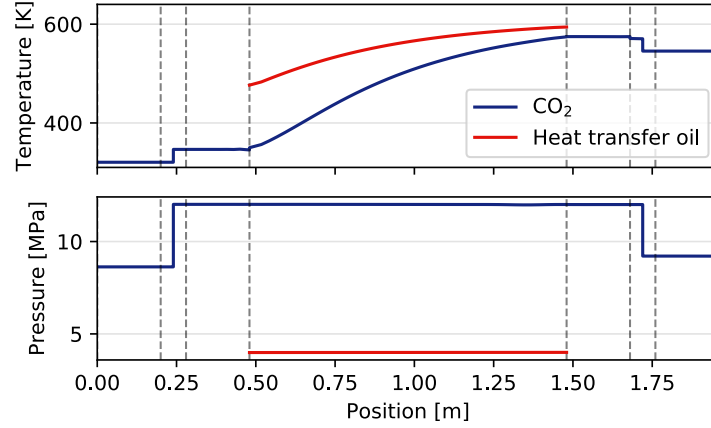


Figure 2: Steady-state temperature and pressure profiles — used as initial conditions for transient simulations — showing pipework (I, III, IV, VI), heat exchanger (IV), compressor (II), and turbine (V).  $\dot{m}_{CO_2} = 10\text{kg/s}$ ,  $\dot{m}_{oil} = 10\text{kg/s}$ .

Table 1: System parameters

Heat exchanger		Pipes	
Length $L$ :	1 m	Length $L$ :	0.2 m
Channel diameter $d$ :	1.0 mm	Diameter $d$ :	0.08 m
Wall thickness $t_w$ :	1.3 mm	$N_{cells}$ (simulation model):	20
Number of channels $N_{chans}$ :	4000		
$N_{cells}$ (simulation model):	100		
Compressor		Turbine	
Model:	See Clementoni et al. [2015]	Model:	Ricardo & Co A70
Maximum efficiency:	0.67	Maximum efficiency:	0.89
Design enthalpy rise:	25.41 kJ/kgK	Design pressure ratio:	1.5
Design mass flow rate:	10 kg/s	Design mass flow parameter:	3.2
Rotational inertia:	0.7 kgm <sup>2</sup>	Design inlet temperature:	600 K

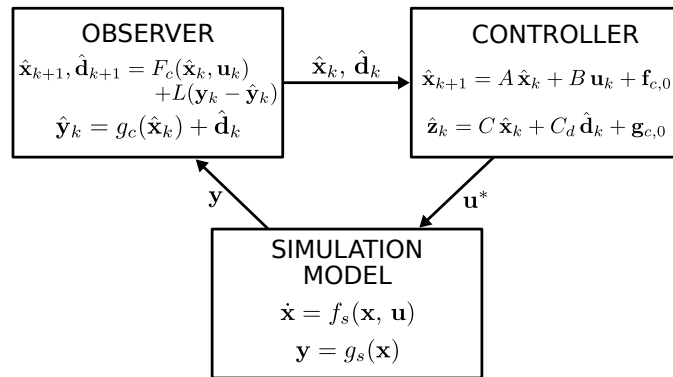


Figure 3: Simulation and control approach (detailed in Sec. 5)

We analyze the performance of the proposed MPC scheme using the closed-loop simulation setup shown in Fig. 3. This setup uses a high-fidelity simulation model (see Sec. 3) with states  $\mathbf{x}$  and measured outputs  $\mathbf{y}$  as a substitute for the real plant. At each sampling instant, the control update procedure is as follows: First, the observer, based on the reduced-order control model (see Sec. 4), generates state estimates  $\hat{\mathbf{x}}$  and disturbance estimates  $\hat{\mathbf{d}}$  from measurements  $\mathbf{y}$ . The controller linearizes the control model about the current operating point  $(\hat{\mathbf{x}}_0, \mathbf{u}_0)$ , then uses this linear model to compute the optimal inputs  $\mathbf{U}^*$  that drive the tracked outputs  $\mathbf{z}$  to their target values. Finally, the first set of optimal inputs  $\mathbf{u}^*$  are applied to the simulation model.

### 3 Simulation model

sCO<sub>2</sub> cycles are an early-stage technology and expensive to construct, so development of new control strategies on real plants is impractical. Accordingly, we develop and test our control strategy using a high-fidelity simulation model that incorporates experimental heat exchanger, compressor, and turbomachinery datasets. Our simulation model is developed using a similar approach as the Argonne National Laboratory Plant Dynamics Code [Moisseytsev and Sienicki, 2007], which is a thoroughly validated [Moisseytsev and Sienicki, 2011, 2012, 2016] dynamic model for sCO<sub>2</sub> cycles (and is not publicly available). This section presents the simulation model, which is developed by combining submodels of five component types — pipes, heat exchangers, turbomachinery, pumps, and boundaries — in the configuration shown in Fig. 1.

#### 3.1 Quasi-1D streams

Submodels for pipes, heat exchangers, and turbomachinery are developed using the quasi-1D stream as a fundamental building block. Being *quasi*-1D, these streams account for the effects of cross-sectional geometry on flow velocity, heat transfer, and pressure drop, and so can be used model components with 3D axially-dominated flow [Carstens, 2007, Moisseytsev and Sienicki, 2007].

We neglect axial conduction within quasi-1D streams as it is negligible for the component types of interest. In printed heat exchangers, transverse thermal gradients are much greater than axial ones, so axial conduction in the fluid can safely be neglected (as shown experimentally in [Bone et al., 2018]). And in turbomachinery, the high axial velocities of the fluid mean that axial conduction is negligible. Under this assumption, the governing equations for quasi-1D flow with heat transfer and frictional pressure drop are

$$A \frac{\partial \rho}{\partial t} = - \frac{\partial(\rho v A)}{\partial x} \quad (3.1a)$$

$$A \frac{\partial(\rho v)}{\partial t} = - \frac{\partial(\rho v |v| A + pA)}{\partial x} - p \frac{\partial A}{\partial x} - \text{fr} \frac{\rho v |v| A}{2D_H} \quad (3.1b)$$

$$A \frac{\partial(\rho E)}{\partial t} = - \frac{\partial(\rho H v A)}{\partial x} - \text{fr} \frac{\rho v^3 A}{2D_H} - q'' \quad (3.1c)$$

where  $t$  is time,  $x$  is the spatial coordinate,  $v$  is velocity,  $p$  is pressure,  $\rho$  is density,  $e$  is specific internal energy, specific enthalpy is  $h = e + p/\rho$ , specific total energy is  $E = e + \frac{1}{2}v^2$ , specific total enthalpy is  $H = h + \frac{1}{2}v^2$ ,  $D_H$  is the hydraulic diameter,  $\text{fr}$  is the Darcy friction factor,  $A$  is the total flow area, and  $q''$  is the heat flux through the wall. These equations are closed using an equation of state for the relevant fluid (see Sec. 3.6). To solve, we integrate Eqs. 3.1 over  $N_{cells}$  finite volumes spanning the computational domain, yielding a system of temporal ODEs for the evolution of density, velocity, and total energy in each volume.

For incompressible working fluids, density and pressure are independent, so the discretized continuity equation (Eq. 3.1a) becomes a constraint on the velocity field, rather than a transport equation for density [Versteeg and Malalasekera, 2007]. In this case, at each timestep, we use the unsteady PISO algorithm [Issa, 1986] with implicit Euler time integration to compute the pressure and velocity fields, and the unsteady energy equation with central differencing to compute the temperature field (consult [Issa, 1986] or [Versteeg and Malalasekera, 2007] for details). The remaining fluid properties are computed from temperature and pressure using the equation of state. We assume that fluid properties are fixed at the inflow boundary and that the flow is fully-developed at the outflow boundary.

For compressible working fluids, we directly solve the governing temporal ODEs using the AUSMDV flux splitting scheme [Wada and Liou, 1997] with 4<sup>th</sup>-order Runge-Kutta Cash-Karp time integration [Cash and Karp, 1990] (refer to the sources for details). To accurately model pressure and mass flow dynamics in fluid streams that are driven by turbomachinery, compressible boundaries must be modeled properly. To replicate the physics of a real system, we model these boundaries by assuming that the fluid flows from some infinitely-large inlet reservoir, through the computational domain, then into an infinitely-large outlet reservoir (see Sec. 3.1.1).

### 3.1.1 Compressible-flow boundary conditions

For compressible fluids, inflow boundaries are modeled by assuming that the fluid isentropically accelerates from a reservoir at some fixed stagnation conditions ( $p_{stag, in}$ ,  $T_{stag, in}$ ) into the computational domain (similar to the subsonic boundary model in [Jacobs and Gollan, 2018]). Fig. 4 shows a schematic of the inflow boundary model.

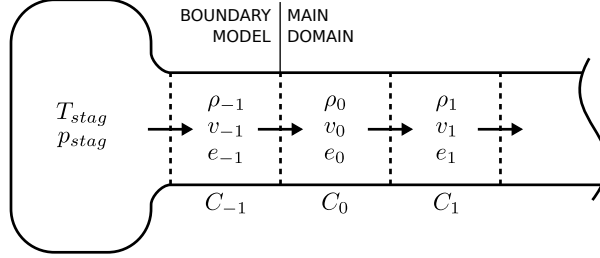


Figure 4: Inflow boundary model

At beginning of each timestep, the boundary model sets the property values in  $C_{-1}$ , allowing  $C_0$  may be treated normally by the compressible flow solver.  $C_{-1}$  is updated as follows. We assume zero velocity gradient over the inflow boundary, and so set

$$v_{-1} = v_0 \quad (3.2)$$

where  $v_{-1}$  and  $v_0$  are the velocities in cells  $C_{-1}$  and  $C_0$  (and  $v_0$  was computed during the previous timestep). Assuming that the fluid accelerates isentropically from the reservoir into  $C_{-1}$ , the enthalpy  $h_{-1}$  is

$$h_{-1} = h_{stag, in} - \frac{v_{-1}^2}{2} \quad (3.3)$$

where  $h_{stag, in} = \text{EOS}(p_{stag, in}, T_{stag, in})$ , and the notation  $w = \text{EOS}(\alpha, \beta)$  means to compute the property  $w$  from properties  $\alpha$  and  $\beta$  using an appropriate equation of state (see Sec. 3.6). From the stagnation entropy,  $s_{stag, in} = \text{EOS}(p_{stag, in}, T_{stag, in})$ , all other properties in  $C_{-1}$  are computed using the equation of state.

For outflow boundaries, we assume that the fluid decelerates from the final cell into the reservoir via a completely irreversible process where all kinetic energy is dissipated. This assumption means that the pressure in the final cell is fixed to the reservoir pressure  $p_{stag, out}$  and the temperature is set by the outgoing fluid temperature. As for the inflow, we compute the outflow velocity using a zero-gradient approximation.

## 3.2 Pipework

Pipes are modeled as quasi-1D streams (Eqs. 3.1) without heat transfer. The well-established Darcy and Colebrook-White [White, 2011] formulae are used to compute the friction factor for laminar and turbulent flow respectively.

## 3.3 Heat exchangers

This article focuses on PCHEs as they are most suitable for the heat addition and recuperation processes in sCO<sub>2</sub> cycles [Musgrove et al., 2017]. PCHEs consist of several layers of metal plates into which zigzag-shaped microchannels have been chemically etched. Alternating hot-stream and cold-stream plates are arranged on top of one another in a counter-flow configuration, then diffusion bonded together to create a solid block [Musgrove et al., 2017].

We develop a plant-level simulation model of a PCHE by following the approach of Carstens [2007] and Moisseytsev and Sienicki [2007]. We assume that 1) mass flow is distributed evenly between all channels, 2) fluid properties in all channels are the same at a given axial distance into the heat exchanger, and 3) all channels have the same geometry. Under these assumptions, PCHEs may be modeled as two representative 1D fluid channels separated by a conductive wall, as illustrated in Fig. 5. Each representative channel is modeled using the quasi-1D flow equations (Eqs. 3.1), where the flow area and heat transfer area  $A_w$  are scaled by the number of channels  $N_{chans}$ . We use the Colebrook-White [White, 2011] formula to compute the friction factor for turbulent flow.

Because (1) axial conduction in PCHE walls is minimal and (2) the thermal resistance for cross-wall conduction is small compared to that for forced convection [Bone et al., 2018], we assume that heat flows through the heat exchanger walls strictly in the transverse direction (see Fig. 5). Under these assumptions, wall temperature dynamics are given by

$$A_w \rho_w C_{p, w} \frac{dT_w}{dt} = q_h'' + q_c'' \quad (3.4)$$

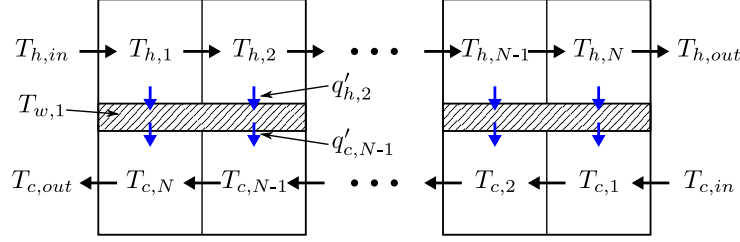


Figure 5: PCHE modelling approach

where  $\rho_w$ ,  $C_{p,w}$ , and  $T_w$  are the density, heat capacity, and mean wall temperature in the transverse direction respectively.  $q''_h$  is the heat flux to the hot stream, given by

$$q''_h = N_{chans} U_h P_h (T_h - T_w) \quad (3.5)$$

where for the hot channel,  $T_h$  is the fluid temperature,  $P_h$  is the wetted perimeter and  $U_h$  is the local heat transfer coefficient (the cold stream heat flux  $q''_c$  is treated analogously). The heat transfer coefficient is computed using the Nusselt number  $Nu$ , the channel's characteristic length  $L_C$ , and the fluid's thermal conductivity  $k$  as, for the hot stream,

$$U_h = Nu_h k_h / L_{C,h}. \quad (3.6)$$

To accurately model heat exchanger behavior, it is crucial to select valid heat transfer correlations that properly account for the effects of channel geometry and multi-dimensional fluid flow [Bone et al., 2018].

### 3.3.1 Heat transfer correlations

Due to its property variations, supercritical CO<sub>2</sub> exhibits complex heat transfer behavior, especially near its critical point. Accurately modelling supercritical CO<sub>2</sub> heat transfer over a wide operating range likely requires several switched heat transfer correlations. However, as this work focuses on control design, we select a heat transfer correlation that gives representative heat transfer behavior of a supercritical CO<sub>2</sub> PCHE near its design point. (Our approach is trivially extensible to cases with switched heat transfer correlations.) Moreover, by fitting the heat exchanger model to small experimental datasets collected from real heat exchangers, heat transfer behavior can be modeled very accurately with only approximate knowledge of internal geometry or heat transfer correlations [Bone et al., 2018].

Flow in the PCHEs in the sCO<sub>2</sub> cycle is typically turbulent, so we use the Ngo-Ishizuka correlation [Ngo et al., 2007] to model supercritical CO<sub>2</sub> heat transfer. This correlation was developed for turbulent flow in channels of hydraulic diameter 1.09 mm and zigzag angle 52° using experimental data, and gives Nusselt number as

$$Nu = 0.1696 Re^{0.629} Pr^{0.317}, \quad (3.7)$$

where  $Re$  is the Reynolds number and  $Pr$  is the Prandtl number.

The thermal oil flow is laminar with  $Re$  typically less than 200. Accordingly, its heat transfer is unlikely to be affected by the zigzag channel geometry, so we model its heat transfer using the analytical correlation for fully-developed laminar flow in a straight semi-circular duct with constant heat flux and transversely invariant properties [Faghri et al., 2010]:

$$Nu = 4.089 \quad (3.8)$$

## 3.4 Turbomachinery

Turbomachinery exhibit complex thermo-fluid behavior that cannot be modeled in detail in a plant-level simulation model. Here, we develop a suitable turbomachinery model following a similar approach to Moisseytsev and Sienicki [2007]. This approach assumes that the thermodynamic response of turbomachines is instantaneous, so their outlet thermodynamic state ( $p_{out}$ ,  $T_{out}$ ) is a function  $f_{tb}$  of only their inlet fluid state ( $p_{in}$ ,  $T_{in}$ ), mass flow rate  $\dot{m}_{tb}$ , and shaft speed  $N_s$ :

$$p_{out}, T_{out} = f_{tb}(p_{in}, T_{in}, \dot{m}_{tb}, N_s). \quad (3.9)$$

Under this assumption, turbomachines may be modeled using either simplified meanline models or performance maps (which may be generated from experiments or CFD [Jahn and Keep, 2017]). This work uses 2D performance maps with analytical off-design scaling (detailed in Appendix A). However, the control strategy proposed in this article works with any turbomachinery model that fits the form of Eq. 3.9. When modelling an operational plant, highly-accurate 4D performance maps would likely be used since detailed operating data would be available.

### 3.4.1 Integration of turbomachinery models into the flow solver

Using performance maps, turbomachines can be modeled as two adjacent compressible flow cells ( $C_{L0}$  and  $C_{R0}$ ) with momentum and energy discontinuities  $\Delta_{mom}$  and  $\Delta_E$  over the interface  $I_C$  that separates them (see Fig. 6). With these discontinuities, the flux vectors on the left and right of  $I_C$  ( $F_L$  and  $F_R$  respectively) are

$$\begin{bmatrix} F_{m,R} \\ F_{mom,R} \\ F_{E,R} \end{bmatrix} = \begin{bmatrix} F_{m,L} \\ F_{mom,L} + \Delta_{mom} \\ F_{E,L} + \Delta_E \end{bmatrix} \quad (3.10)$$

where the subscripts  $m$ ,  $mom$ , and  $E$  refer to mass, momentum, and energy. During gas dynamic updates, cell  $C_{L0}$  is integrated using  $F_L$  and the flux vector at  $I_{L0}$ , similarly  $C_{R0}$  is integrated using  $F_R$  the flux vector at  $I_{R0}$ . The discontinuities  $\Delta_{mom}$  and  $\Delta_E$  are not directly computed; they emerge from the process used to compute  $F_L$  and  $F_R$  from the turbomachinery maps.

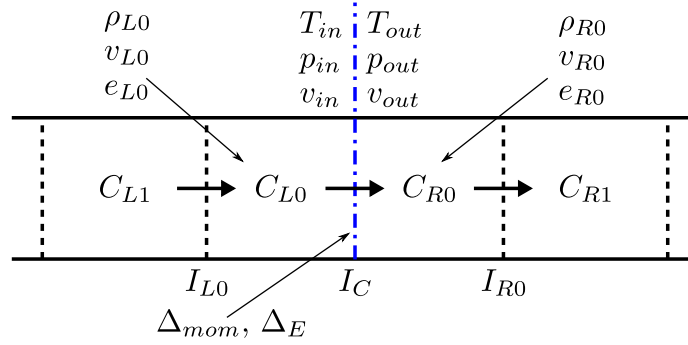


Figure 6: Turbomachinery modelling concept

Because (1) mass flow rate through a turbomachine is primarily governed by pressure ratio and (2) off-design scaling is performed based on the inlet fluid state, we reformulate the performance maps as a function of pressure ratio [Moissevsev and Sienicki, 2007]:

$$T_{out}, \dot{m}_{tb} = f'_{tb}(p_{in}, p_{out}, T_{in}, N_s). \quad (3.11)$$

Using these reformulated performance maps,  $F_L$  and  $F_R$  are calculated as follows. First, the shaft speed is updated from rotordynamics (see Appendix Sec. 3.4.2). Next, from the current fluid states in  $C_{L0}$  and  $C_{R0}$  we set

$$T_{in} = T_{L0}, \quad p_{in} = p_{L0}, \quad p_{out} = p_{R0}. \quad (3.12)$$

Then, we compute  $T_{out}$  and  $\dot{m}_{tb}$  from the performance maps (see Appendix A), then compute the inlet and outlet velocities  $v_{in}$  and  $v_{out}$  and shaft work  $\dot{W}$  as

$$v_{in} = \dot{m}_{tb} / (A_{tb,in} \rho_{in}), \quad (3.13)$$

$$v_{out} = \dot{m}_{tb} / (A_{tb,out} \rho_{out}), \quad (3.14)$$

$$\dot{W} = \dot{m}_{tb} (h_{out} - h_{in} + 1/2 (v_{out}^2 - v_{in}^2)), \quad (3.15)$$

where  $A_{tb,in}$  and  $A_{tb,out}$  are the inlet and outlet flow areas of the turbomachine. This solution approach implicitly captures efficiency from the turbomachinery maps. Finally, the flux vectors are formed as

$$F_L = \begin{bmatrix} \dot{m}_{tb}/A_{tb,in} \\ (\dot{m}_{tb} v_{in}/A_{tb,in}) + p_{in} \\ (\dot{m}_{tb} E_{in}/A_{tb,in}) \end{bmatrix} \quad (3.16)$$

and

$$F_R = \begin{bmatrix} \dot{m}_{tb}/A_{tb,out} \\ (\dot{m}_{tb} v_{out}/A_{tb,out}) + p_{out} \\ (\dot{m}_{tb} E_{in}/A_{tb,in}) - \dot{W}_s \end{bmatrix}. \quad (3.17)$$

When evaluating interfaces fluxes for  $I_{L0}$  and  $I_{R0}$ , ghost cells populated with first-order extrapolation are used to prevent the compressible flux calculator from ‘looking over’ the momentum and energy discontinuity at  $I_C$ .



### 3.4.2 Turbomachinery rotor dynamics

Turbomachines may be either synchronous (grid-connected at some constant speed  $N_{s0}$ ) or asynchronous (variable-speed). The rotational dynamics of asynchronous turbomachines depend on the load and external torques ( $T_{load}$  and  $T_{external}$ ). For compressors,  $T_{external}$  is the applied motor torque, and for turbines,  $T_{external}$  is the supplied generator torque. The load torque is

$$T_{load} = \dot{W}_s / N_s, \quad (3.18)$$

where  $\dot{W}_s$  is computed using performance maps (see Appendix A) and Eq. 3.15. (see Appendix A), Using these torques, turbomachinery rotational dynamics are given by

$$J \frac{dN_s}{dt} = T_{external} - T_{load}. \quad (3.19)$$

where  $J$  is the moment of inertia of the turbomachine’s rotor plus connected rotating masses (such as gearbox components).

### 3.5 Thermal oil pump

The mass flow rate in the thermal oil stream  $\dot{m}_{oil}$  is set by a pump. We assume that the fluid exits the pump at  $T_{oil,in} = 300$  °C and  $p_{oil,in} = 4$  MPa, and we assume that a PID controller modulates pump speed such that  $\dot{m}_{oil}$  is driven towards the setpoint  $\dot{m}_{oil,ref}$ . We assume that the local closed-loop dynamics of the pump and controller subsystem are

$$J_p \frac{d^2 \dot{m}_{oil}}{dt^2} = k_p (\dot{m}_{oil,ref} - \dot{m}_{oil}) - c_p \frac{d\dot{m}}{dt}, \quad (3.20)$$

where  $J_p$ ,  $c_p$ , and  $k_p$  are the effective inertia, damping coefficient, and stiffness respectively. We assume that the PID gains are set such that the pump and controller subsystem has a natural frequency of 2 Hz and slightly overdamped response, with damping ratio 1.3.

### 3.6 Fluid property calculations

We form fluid property lookup tables using the open-source fluid property database CoolProp [Bell et al., 2014]. CoolProp computes CO<sub>2</sub>’s thermodynamic state by iteratively solving the Span and Wagner equation of state [Span and Wagner, 1996], and computes its thermal conductivity and viscosity using the Scalabrin et. al. [Scalabrin et al., 2006] and Fenghour et. al. [Fenghour et al., 1998] correlations respectively. CoolProp models Paratherm™HE using an incompressible equation of state based on manufacturer data [par].

For computational efficiency, we compute fluid properties from the lookup tables using bicubic interpolation. Discontinuous approximation methods (such as tabular Taylor series extrapolation) make the compressor performance map model used in this article ill-conditioned and thus cannot be used.

## 4 Control model

The simulation model presented in Sec. 3 is ill-suited for control applications due to its high state dimension and stringent explicit timestep restrictions, imposed by the Courant-Friedrichs-Lewy condition [Courant et al., 1967]. This section discusses the formulation of a simpler control model of the open sCO<sub>2</sub> cycle (detailed in Sec. 2). This control model (denoted by  $f_c$  and  $g_c$  in Fig. 3), is linearized online to implement MPC and is also used to estimate unmeasured states. The control model is primarily composed of two submodels: one for the thermal and bulk-flow dynamics in non-ideal fluid streams (used for both the CO<sub>2</sub> and thermal oil streams), and one for the slow-timescale pressure and mass flow dynamics in the CO<sub>2</sub> stream.

Previous work [Bone et al., 2019] shows that by assuming the momentum dynamics in compressible fluid streams are infinitely-fast (the ‘quasi-steady-momentum’ assumption), these streams can be modeled using quasi-incompressible flow equations, which capture only the slow-timescale energy and bulk-flow dynamics. This work shows that the quasi-steady-momentum assumption can also be used to derive a control model for the pressure and mass flow dynamics in compressible flow systems that are driven by turbomachinery behavior and heat transfer dynamics.

### 4.1 Turbomachinery rotor dynamics

In the control model, the rotordynamics of asynchronous turbomachines are modeled by linearizing Eq. 3.19 about the current operating point. The load torque is computed using the performance map model, and so can be considered as

a function  $T_{load}(p_{in}, p_{out}, T_{in}, N_s)$ . For the compressor, with  $T_{external}$  as the motor torque  $T_m$ , the linearization of Eq. 3.19 is

$$J_c \frac{dN_c}{dt} = T_{m,0} + \bar{T}_m - T_{load,0} - \frac{\partial T_{load}}{\partial N_c} \bar{N}_c - \frac{\partial T_{load}}{\partial \dot{m}_c} \bar{\dot{m}}_c - \frac{\partial T_{load}}{\partial T_{c,in}} \bar{T}_{c,in} - \frac{\partial T_{load}}{\partial p_{c,in}} \bar{p}_{c,in}. \quad (4.1)$$

where the ‘overbar’ variables represent deviation from the linearization point and ‘subscript 0’ variables denote values at the linearization point (see Sec. 5.2). As discussed in in Sec. 4.4, in the control model, the compressor inlet temperature and pressure are considered fixed, so Eq. 4.1 can be simplified to

$$J_c \frac{dN_c}{dt} = T_{m,0} + \bar{T}_m - T_{load,0} - \frac{\partial T_{load}}{\partial N_c} \bar{N}_c - \frac{\partial T_{load}}{\partial \dot{m}_c} \bar{\dot{m}}_c. \quad (4.2)$$

## 4.2 Heat exchanger walls

The simulation model for the heat exchanger walls is appropriate for control without further simplification. Integrating Eq. 3.4 over  $N_{cells}$  volumes yields the following temporal ODE for temperature in wall cell  $i$ :

$$A_w \rho_w C_{p,w} \frac{dT_{w,i}}{dt} = N_{chans} (U_h P_{C,h} (T_{h,i} - T_{w,i}) + U_c P_{C,c} (T_{c,i} - T_{w,i})) \quad (4.3)$$

where  $T_{h,i}, T_{c,i}$  are the neighboring hot-stream and cold-stream fluid cells, and the heat transfer coefficients  $U_c$  and  $U_h$  are given by Eq. 3.6. Eq. 4.3 is linearized online to implement MPC (see Sec. 5.2). Best closed-loop performance was obtained by retaining only the ‘primary’ partial derivatives in the linearization, giving

$$\frac{dT_{w,i}}{dt} \approx \frac{N_{chans}}{A_w \rho_w C_{p,w}} \left( \frac{dT_{w,i,0}}{dt} - (U_h P_{C,h} + U_c P_{C,c}) \bar{T}_{w,i} + U_h P_{C,h} \bar{T}_{h,i} + U_c P_{C,c} \bar{T}_{c,i} \right), \quad (4.4)$$

where  $\frac{dT_{w,i,0}}{dt}$  is the derivative of wall temperature at the linearization point.

## 4.3 Fluid streams

For control, we model only the slow-timescale dynamics (the thermal and bulk-flow dynamics) of quasi-1D streams [Bone et al., 2019] by applying the quasi-steady momentum assumption,

$$\frac{\partial(\rho v)}{\partial t} \approx 0, \quad (4.5)$$

to the quasi-1D flow equations (Eqs. 3.1). This assumption effectively states that the momentum dynamics (i.e. pressure waves) stabilize infinitely quickly compared to the other dynamics. For the operating conditions considered in this article, this assumption is justified as Mach numbers in the CO<sub>2</sub> stream are always less than 0.01, so the pressure wave characteristics are much faster than the bulk-flow characteristic [Bone et al., 2019]. Similarly low Mach number ranges have been observed in experimental tests of supercritical CO<sub>2</sub> heat exchangers [Bone et al., 2018].

Additionally, we make two more assumptions: (1) that the pressure changes throughout the fluid streams are negligible except over the turbomachinery (see Sec. 4.4), and (2) that  $H \approx h$  and  $E \approx e$  (as flow velocities are typically small in the heat exchanger channels used for sCO<sub>2</sub> cycles [Bone et al., 2018]). By applying these assumptions to Eqs. 3.1 then combining Eqs. 3.1a and 3.1c, the energy dynamics of a fluid streams are given by Bone et al. [2019]

$$\rho \frac{\partial e}{\partial t} = -\frac{\partial(\rho h v)}{\partial x} - \frac{q''}{A}, \quad (4.6)$$

where the pressure and mass flow rate are set by the stream inlet conditions:  $p = p_{in}$  and  $\dot{m} = \dot{m}_{in}$ . To obtain a temporal ODE for stream internal energy in cell  $i$ , we integrate Eq. 4.6 over  $N_{cells}$  finite volumes, then apply upwind differencing, giving

$$\rho_i \frac{de_i}{dt} = \frac{\dot{m}_{in} (h_{i-1} - h_i)}{A \Delta x} - \frac{N_{chans} \pi \text{Nu} k_i}{A} (T_i - T_{w,i}). \quad (4.7)$$

(See Sec. 3.3.1 for Nusselt number correlations.) For the thermal oil stream,  $p_{in}$  and  $\dot{m}_{in}$  are set by the pump, and for the CO<sub>2</sub> stream,  $p_{in}$  and  $\dot{m}_{in}$  are given by the compressor outflow conditions, which in the control model are captured by the equations presented in Sec. 4.4. As for the walls, best closed-loop performance was obtained when retaining only the primary partial derivatives in the linearization of Eq. 4.7:

$$\begin{aligned} \rho_{i,0} \frac{de_i}{dt} \approx & \frac{(h_{i-1,0} - h_{i,0}) \bar{m}_{in}}{A \Delta x} \\ & + \frac{\dot{m}_{in,0}}{A \Delta x} \left( \frac{\partial h}{\partial e_{i-1,0}} \bar{e}_{i-1} - \frac{\partial h}{\partial e_{i,0}} \bar{e}_i \right) \\ & - \frac{\dot{m}_{in,0} (h_{i-1,0} - h_{i,0})}{\rho_{i,0} A \Delta x} \frac{\partial \rho}{\partial e_{i,0}} \bar{e}_i \\ & - \frac{N_{chans} \pi \text{Nu} k_{i,0}}{\rho_{i,0} A} \left( \frac{\partial T}{\partial e_{i,0}} \bar{e}_i - \bar{T}_{w,i} \right). \end{aligned} \quad (4.8)$$

#### 4.4 Mass flow rate and pressure modelling

MPC requires a low-order model for the slow-timescale evolution of mass flow rate and high-side pressure in the system. This section derives such a model by applying the quasi-steady momentum assumption, performing system-level mass and momentum balances, and approximating turbomachinery performance with Taylor series expansions.

First, we perform a system-level momentum balance to relate the turbomachinery mass flow rates to compressor speed. For the CO<sub>2</sub> stream, the pressure difference between the reservoirs is equal to the total pressure change over the system:

$$p_{stag,in} - p_{stag,out} = \Delta p_{pipes} + \Delta p_{HX,CO_2} + \Delta p_c + \Delta p_t \quad (4.9)$$

where the pressure changes over the turbomachinery are

$$\Delta p_c = p_{out,c} - p_{in,c} \quad \text{and} \quad \Delta p_t = p_{out,t} - p_{in,t}. \quad (4.10)$$

Assuming the pressure drops over the pipes and heat exchanger ( $\Delta p_{pipes}$  and  $\Delta p_{HX,CO_2}$ ) are negligible, the low-side pressures are fixed to the reservoir pressures ( $p_{c,in} = p_{stag,in}$ ,  $p_{t,out} = p_{stag,out}$ ), so

$$p_{stag,in} - p_{stag,out} = \Delta p_c + \Delta p_t \quad (4.11)$$

and

$$p_{high} \equiv p_{c,out} \equiv p_{t,in}. \quad (4.12)$$

As the low-side pressures are fixed, we reformulate the turbine performance map model (Eq. 3.9) with  $p_{t,out}$  as an input and  $p_{t,in}$  as an output, giving

$$\begin{aligned} \Delta p_c, T_{out,c} &= g_{comp}(p_{in,c}, T_{in,c}, \dot{m}_c, N_c) \\ \Delta p_t, T_{out,t} &= g_{turb}(p_{out,t}, T_{in,t}, \dot{m}_t, N_t). \end{aligned} \quad (4.13)$$

Noting that (1)  $p_{in,c}$  and  $T_{in,c}$  are fixed to the inlet reservoir conditions, (2)  $p_{out,t}$  is fixed to the outlet reservoir temperature, and (3)  $N_t$  is fixed to the synchronous speed, a first-order Taylor series expansion of  $g_{comp}$  and  $g_{turb}$  about the current operating point yields

$$\Delta p_c \approx \Delta p_{c,0} + \frac{\partial \Delta p_c}{\partial \dot{m}_c} \bar{m}_c + \frac{\partial \Delta p_c}{\partial N_c} \bar{N}_c \quad (4.14)$$

$$\Delta p_t \approx \Delta p_{t,0} + \frac{\partial \Delta p_t}{\partial T_{in,t}} \bar{T}_{in,t} + \frac{\partial \Delta p_t}{\partial \dot{m}_t} \bar{m}_t, \quad (4.15)$$

where  $\frac{\partial \Delta p_c}{\partial p_{in,c}}$  refers to the partial derivative of  $g_{comp}$  with respect to  $p_{in,c}$  considering the output variable  $\Delta p_c$  (and similar for the other partial derivatives).

Substituting Eqs. 4.14 and 4.15 into Eq. 4.11 yields

$$\begin{aligned} p_{stag,in} - p_{stag,out} &= \Delta p_{c,0} + \frac{\partial \Delta p_c}{\partial \dot{m}_c} \bar{m}_c + \frac{\partial \Delta p_c}{\partial N_c} \bar{N}_c \\ &+ \Delta p_{t,0} + \frac{\partial \Delta p_t}{\partial T_{in,t}} \bar{T}_{in,t} + \frac{\partial \Delta p_t}{\partial \dot{m}_t} \bar{m}_t. \end{aligned} \quad (4.16)$$

As the pressure change between the reservoirs must be equal to the pressure change over the turbomachinery at the linearization point (i.e.  $p_{stag, in} - p_{stag, out} = \Delta p_{c,0} + \Delta p_{t,0}$ ), Eq. 4.16 can be simplified to

$$0 = \frac{\partial \Delta p_c}{\partial \dot{m}_c} \bar{m}_c + \frac{\partial \Delta p_c}{\partial N_c} \bar{N}_c + \frac{\partial \Delta p_t}{\partial T_{in,t}} \bar{T}_{in,t} + \frac{\partial \Delta p_t}{\partial \dot{m}_t} \bar{\dot{m}}_t. \quad (4.17)$$

Turbine inlet temperature has only a small effect on high-side pressure, with the product  $\frac{\partial \Delta p_t}{\partial T_{in,t}} \bar{T}_{in,t}$  typically being around three orders of magnitude less than the other terms. Neglecting this term and differentiating Eq. 4.17 with respect to time gives the compressor mass flow dynamics as

$$\frac{d\dot{m}_c}{dt} = -\frac{\partial \dot{m}_c}{\partial \Delta p_c} \left( \frac{\partial \Delta p_c}{\partial N_c} \frac{dN_c}{dt} + \frac{\partial \Delta p_t}{\partial \dot{m}_t} \frac{d\dot{m}_t}{dt} \right), \quad (4.18)$$

where by definition  $\frac{d\bar{N}_c}{dt} = \frac{dN_c}{dt}$  and the same for all other perturbed variables. Eq. 4.18 is used to model compressor mass flow dynamics by substituting the equations for compressor shaft speed dynamics (Eq. 4.2) and turbine mass flow dynamics (Eq. 4.28).

Next, we develop an equation for turbine mass flow rate by applying the conservation of mass to the high-pressure side of the system. The fluid mass in the high-pressure side is

$$m_{high} = \sum_{i=1}^{N_{cells, high}} \rho_i V_i, \quad (4.19)$$

where  $N_{cells, high}$  is the number of cells in the high-pressure side. Additionally, the rate that fluid mass accumulates in the high-pressure side of the system is the difference between the compressor and turbine mass flow rates:

$$\frac{dm_{high}}{dt} = \dot{m}_c - \dot{m}_t. \quad (4.20)$$

As cell volume is constant, differentiating Eq. 4.19 with respect to time yields

$$\frac{dm_{high}}{dt} = \sum_{i=1}^{N_{cells, high}} \frac{d\rho_i}{dt} V_i. \quad (4.21)$$

Choosing thermodynamic state variables of  $\rho$  and  $e$ , Eq. 4.21 can be expanded as

$$\frac{dm_{high}}{dt} = \sum_{i=1}^{N_{cells, high}} V_i \left( \frac{\partial \rho}{\partial e} \Big|_{p=p_i, e=e_i} \frac{de_i}{dt} + \frac{\partial \rho}{\partial p} \Big|_{p=p_i, e=e_i} \frac{dp_i}{dt} \right), \quad (4.22)$$

where  $p_{i,0}$  and  $e_{i,0}$  are the pressures and internal energies in cell  $i$  at the current operating point. Because we assume the high-side pressure to be uniform, Eq. 4.22 can be simplified as

$$\begin{aligned} \frac{dm_{high}}{dt} &= \left( \sum_{i=1}^{N_{cells, high}} V_i \frac{\partial \rho}{\partial e} \Big|_{p=p_{high}, e=e_i} \frac{de_i}{dt} \right) \\ &+ \left( \sum_{i=1}^{N_{cells, high}} V_i \frac{\partial \rho}{\partial p} \Big|_{p=p_{high}, e=e_i} \right) \frac{dp_{high}}{dt}. \end{aligned} \quad (4.23)$$

From Eqs. 4.10 and 4.12, the time derivatives of  $\Delta p_t$  and  $p_{high}$  are related as follows:

$$\frac{d}{dt} \Delta p_t = \frac{d}{dt} (p_{out,t} - p_{in,t}), \quad (4.24)$$

so

$$\frac{dp_{high}}{dt} = -\frac{d\Delta p_t}{dt}. \quad (4.25)$$

Deriving the Taylor series approximation for  $\Delta p_t$  (Eq. 4.15) with respect to time and substituting into Eq. 4.25, gives

$$\frac{dp_{high}}{dt} = -\frac{\partial \Delta p_t}{\partial T_{in,t}} \frac{dT_{in,t}}{dt} - \frac{\partial \Delta p_t}{\partial \dot{m}_t} \frac{d\dot{m}_t}{dt}. \quad (4.26)$$

As discussed, turbine pressure ratio is not strongly influenced by inlet pressure, so we assume

$$\frac{dp_{high}}{dt} = -\frac{\partial \Delta p_t}{\partial \dot{m}_t} \frac{d\dot{m}_t}{dt}. \quad (4.27)$$

Combining Eqs. 4.23 and 4.27, substituting into Eq. 4.20, then rearranging gives the turbine mass flow dynamics as

$$\begin{aligned} \frac{d\dot{m}_t}{dt} = & \left( \frac{\partial \Delta p_t}{\partial \dot{m}_t} \sum_{i=1}^{N_{cells, high}} V_i \frac{\partial \rho}{\partial p} \Big|_{\substack{p=p_{high} \\ e=e_i}} \right)^{-1} \\ & \times \left( \dot{m}_t - \dot{m}_c + \sum_{i=1}^{N_{cells, high}} V_i \frac{\partial \rho}{\partial e} \Big|_{\substack{p=p_{high} \\ e=e_i}} \frac{de_i}{dt} \right). \end{aligned} \quad (4.28)$$

Due to the damping effect of component wall thermal inertia, the dynamics of internal energy are slower than those for mass flow rate and pressure. Accordingly, we model turbine mass flow dynamics by substituting the current values of internal energy time derivatives  $\frac{de_i}{dt}_0$  into Eq. 4.28.

This concludes development of the control dynamics model. This model comprises equations for the dynamics of wall temperature (Eq. 4.3), fluid stream internal energy (Eq. 4.7), mass flow rates and pressure in the CO<sub>2</sub> stream (Eqs. 4.18, 4.28, 4.27), compressor shaft speed (Eq. 4.1), and thermal oil pump system (Eq. 3.20).

#### 4.5 Output model — net power and turbine inlet temperature

For the control problem defined in Sec. 2, the tracked-outputs are net power output and turbine inlet temperature. Choosing thermodynamic state variables of  $p$  and  $e$ , turbine inlet temperature can be approximated from  $p_{high}$  and the final-cell high-side internal energy  $e_{N_{cells, high}}$  as

$$\bar{T}_{in, t} = T_{in, t, 0} + \frac{\partial T}{\partial e} \Big|_{\substack{p=p_{high} \\ e=e_{in, t}}} \bar{e}_{in, t} + \frac{\partial T}{\partial p} \Big|_{\substack{p=p_{high} \\ e=e_{in, t}}} \bar{p}_{high}, \quad (4.29)$$

where  $T_{in, t, 0}$  is the most recent measurement of turbine inlet temperature. For the open sCO<sub>2</sub> cycle, the net power output is

$$\dot{W}_{net} = \dot{W}_t - \dot{W}_c. \quad (4.30)$$

Linearizing the performance maps and discarding negligible terms (as for  $\Delta p_c$  and  $\Delta p_t$ ) yields

$$\begin{aligned} \dot{W}_{net} = & \dot{W}_{t, 0} - \dot{W}_{c, 0} + \frac{\partial \dot{W}_t}{\partial T_{in, t}} \bar{T}_{in, t} + \frac{\partial \dot{W}_t}{\partial \dot{m}_t} \bar{\dot{m}}_t \\ & - \frac{\partial \dot{W}_c}{\partial \dot{m}_c} \bar{\dot{m}}_c - \frac{\partial \dot{W}_c}{\partial N_c} \bar{N}_c. \end{aligned} \quad (4.31)$$

Turbine inlet temperature has a significant effect on shaft power and so must be retained in Eq. 4.31.

#### 4.6 Compressor speed constraints

The compressor is subject to minimum and maximum speed constraints. The maximum speed  $N_{c, max}$  is dictated by the shaft bearings and is taken as 126% of the nominal compressor speed based on manufacturer data. Applying some constraint margin  $k_{N, max}$ , the maximum compressor speed is

$$N_c \leq (1 - k_{N, max}) N_{c, max}. \quad (4.32)$$

Minimum compressor speed is dictated by surge: a damaging physical phenomenon, characterized by oscillatory or reversed flow, which occurs when the compressor cannot achieve the required pressure ratio. This section shows how to compute the surge conditions for a given pair of turbomachines. We consider only the case where the turbine operates at a fixed synchronous speed  $N_{t0}$ .

In the control model, the compressor and turbine both have the same high-side pressure  $p_{high} \equiv p_{out, c} \equiv p_{in, t}$ , and at steady-state, they both have the same mass flow rate  $\dot{m}_{sys} \equiv \dot{m}_c \equiv \dot{m}_t$ . The low-side pressures are fixed, so for given shaft speeds and inlet temperatures, the feasible system mass flow rates are given by the intersections of the  $\dot{m}$  versus  $p_{high}$  curves for the two turbomachines. Fig. 7 shows some sample  $\dot{m}$  versus  $p_{high}$  curves, with the feasible mass flow rates  $\dot{m}_1$  and  $\dot{m}_2$  marked. As we employ surge control with a margin, the system is forced to operate at  $\dot{m}_2$ .

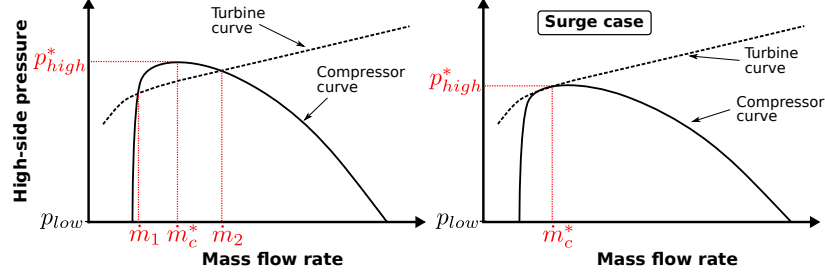


Figure 7: High-side pressure versus mass flow curves for both turbomachines.

Surge conditions can be computed by considering the effect of varying compressor speed. As compressor speed decreases, the maximum achievable high-side pressure  $p_{high}^*$  drops. Surge occurs at the minimum feasible compressor speed  $N_{c, min}$ , where the compressor and turbine  $p_{high}$  versus  $\dot{m}$  curves intersect only at  $p_{high}^*$  (as illustrated on the right side of Fig. 7). Below this speed, the compressor cannot supply the high-side pressure required by the turbine at any mass flow rate, causing surge.

$N_{c, min}$  is operating-point dependent and can be computed online using the following procedure. For the chosen compressor maps (see A.1), we store the combinations of mass flow rate and corrected speed that maximize the compressor outlet pressure, then store these values in lookup tables  $p_{high}^* = f_{c1}(N_{cor})$  and  $\dot{m}_c^* = f_{c2}(N_{cor})$ . For the chosen turbine map model, the high-side pressure  $p_{high} = p_{in, t}$  can be computed from Eq. A.3 as

$$p_{high} = p_{out, t} M_{t1} \left( \dot{m}_t \sqrt{T_{in, t}} / p_{in, t} \right). \quad (4.33)$$

Assuming that the current difference between the turbine and compressor mass flow rates  $\Delta\dot{m}$  persists, the mass flow rate at the turbine when the compressor achieves  $p_{high}^*$  is  $\dot{m}_t^* = \dot{m}_c^* + \Delta\dot{m}$ . Surge occurs when the maximum compressor outlet pressure equals the turbine inlet pressure ( $p_{high}^* = p_{high}$ ):

$$f_{c1}(N_{cor}) = p_{out, t} M_{t1} \left( \dot{m}_t^* \sqrt{T_{in, t}} / p_{in, t} \right) \quad (4.34)$$

To solve for  $N_{c, min}$ , we note that  $p_{in, t} = p_{high}^*$ , substitute Eq. A.17 into Eq. 4.34, then reformulate to give

$$0 = f_{c1}(N_{cor}) - p_{out, t} M_{t1} \left( \frac{\sqrt{T_{in, t}}}{f_{c1}(N_{cor})} (f_{c2}(N_{cor}) + \Delta\dot{m}) \right). \quad (4.35)$$

We compute  $N_{cor, min}$  for the current values of  $p_{out, t}$ ,  $\Delta\dot{m}$ , and  $T_{in, t}$  by solving the root-finding problem defined by Eq. 4.35, then compute the actual minimum speed  $N_{c, min}$  using Eq. A.9.

To prevent surge, we impose the minimum speed constraint

$$N_c \geq (1 + k_{N, min}) N_{c, min, 0} \quad (4.36)$$

where  $N_{c, min, 0}$  is the minimum speed for the current operating point,  $k_{N, min}$  is the constraint margin, and the partial derivatives are computed using finite differences from Eq. 4.35. Again, turbine inlet temperature is approximated using Eq. 4.29. We set  $k_{N, min} = 5\%$  and  $k_{N, max} = 5\%$ .

## 5 Controller design

This section presents an MPC scheme that regulates the net power output  $\dot{W}_{net}$  of the open sCO<sub>2</sub> cycle (see Sec. 2) to  $\dot{W}_{net, ref}$ , while driving the turbine inlet temperature to the target point  $T_{in, t, ref}$ . To maximize the system's thermodynamic efficiency,  $T_{in, t, ref}$  is set as the maximum feasible turbine inlet temperature for the net power  $\dot{W}_{net, ref}$ . The control inputs are the reference flow rate of the thermal oil pump  $\dot{m}_{oil, ref}$  and the compressor motor torque  $T_m$ , which are parametrized using zeroth-order and first-order holds respectively.

### 5.1 State-space form

To implement MPC, we cast the control model in explicit state-space form:

$$\begin{aligned} \frac{dx}{dt} &= f_c(\mathbf{x}, \mathbf{u}) \\ \mathbf{z} &= g_c(\mathbf{x}, \mathbf{u}) \end{aligned} \quad (5.1)$$

where  $\mathbf{x} \in \mathbb{R}^n$ ,  $\mathbf{u} \in \mathbb{R}^m$ , and  $\mathbf{z} \in \mathbb{R}^l$  are the state, input, and tracked-output vectors respectively, and  $f_c : \mathbb{R}^n \times \mathbb{R}^m \rightarrow \mathbb{R}^n$  and  $g_c : \mathbb{R}^n \times \mathbb{R}^m \rightarrow \mathbb{R}^l$  represent the nonlinear dynamics and output control models respectively. The input, tracked-output, and reference vectors are

$$\begin{aligned}\mathbf{u} &= [\dot{T}_m, \dot{m}_{oil,ref}]^\top \\ \mathbf{z} &= [\dot{W}_{net}, T_{in,t}]^\top \\ \mathbf{r} &= [\dot{W}_{net,ref}, T_{in,t,ref}]^\top.\end{aligned}\quad (5.2)$$

$f_c$  comprises equations for the dynamics of internal energy in the fluid streams (Eq. 4.7), wall temperature (Eq. 4.3), mass flow rates and pressure in the CO<sub>2</sub> stream (Eqs. 4.18, 4.28, and 4.27), the compressor shaft speed (Eq. 4.1), and the thermal oil pump system (Eq. 3.20). We choose thermodynamic state variables of density and pressure (and compute all other thermodynamic properties using the equation of state), so the state vector is

$$\mathbf{x} = [\mathbf{T}_{wall}^\top, \mathbf{e}_{CO_2}^\top, p_{high}, \dot{m}_c, \dot{m}_t, N_c, \mathbf{e}_{oil}^\top, \dot{m}_{oil}]^\top, \quad (5.3)$$

where  $\mathbf{T}_{wall} = [T_{wall,1}, \dots, T_{wall,N_{cells,HX}}]^\top$ ,  $\mathbf{e}_{CO_2} = [e_{CO_2,1}, \dots, e_{CO_2,N_{cells}}]^\top$ , and  $\mathbf{e}_{oil} = [e_{oil,1}, \dots, e_{oil,N_{cells,HX}}]^\top$ .  $g_c$  comprises the equations for  $T_{in,t}$  and  $\dot{W}_{net}$  (Eqs. 4.29 and 4.31).

## 5.2 Linearization and discrete-time conversion

We linearize the control model online about the current operating point  $(\mathbf{x}_0, \mathbf{u}_0)$  so that the control updates can be computed using a quadratic programming (QP) solver. Using perturbed variables  $\mathbf{x}' = \mathbf{x} - \mathbf{x}_0$  and  $\mathbf{u}' = \mathbf{u} - \mathbf{u}_0$ , a local linear time-invariant model is given by

$$\begin{aligned}\frac{d\mathbf{x}}{dt} &= A\mathbf{x}' + B\mathbf{u}' + \mathbf{f}_0 \\ \mathbf{z} &= C\mathbf{x}' + D\mathbf{u}' + \mathbf{g}_0,\end{aligned}\quad (5.4)$$

where  $A$ ,  $B$ ,  $C$ ,  $D$  represent the Jacobian matrices of  $f_c$  and  $g_c$  with respect to  $\mathbf{x}$  and  $\mathbf{u}$ ,  $\mathbf{f}_0 = f_c(\mathbf{x}_0, \mathbf{u}_0)$ , and  $\mathbf{g}_0 = g_c(\mathbf{x}_0, \mathbf{u}_0)$ .  $D$  is always zero and thus neglected from now on. Only certain terms are retained in the linearized dynamics equations for heat exchanger wall temperature stream internal energy and (see Eqs. 4.4 and 4.8). We implement MPC with a discrete-time version of Eq. 5.4 with sampling time  $\Delta t$ ,

$$\begin{aligned}\mathbf{x}'_{k+1} &= A_d \mathbf{x}'_k + B_d \mathbf{u}'_k + \mathbf{f}_{0,d} \\ \mathbf{z}_k &= C \mathbf{x}'_k + \mathbf{g}_0,\end{aligned}\quad (5.5)$$

where [Franklin et al., 1990]

$$\begin{aligned}A_d &= \exp(A \Delta t) \\ \Gamma &= \int_0^{\Delta t} \exp(A(\Delta t - \tau)) d\tau I \\ B_d &= \Gamma B, \quad \mathbf{f}_{0,d} = \Gamma \mathbf{f}_0\end{aligned}\quad (5.6)$$

The matrix exponentials are computed using the scaling and squaring method [Higham, 2005]. In the controller, Eq. 5.5 is augmented with an output disturbance model for offset-free reference tracking (see Eq. 5.18).

## 5.3 State estimation

To implement MPC, we require an estimate  $\hat{\mathbf{x}}$  of the state vector  $\mathbf{x}$ . We assume that the mass flow rates, turbomachinery speeds, and high-side pressure are directly measurable. However, the states inside the heat exchanger (the internal energies and wall temperatures) are not measurable, so we estimate these states

$$\mathbf{x}_e = [\mathbf{T}_{wall}^\top, \mathbf{e}_{CO_2}^\top, \mathbf{e}_{oil}^\top]^\top \quad (5.7)$$

with an observer using measurements of the inlet and outlet fluid temperatures of each stream

$$\mathbf{y} = [T_{CO_2,in}, T_{CO_2,out}, T_{oil,in}, T_{oil,out}]^\top, \quad (5.8)$$

where  $\mathbf{y} \in \mathbb{R}^l$ . We estimate  $\mathbf{x}_e$  using a reduced submodel that describes the dynamics of wall temperature (Eq. 4.3) and fluid stream internal energy (Eq. 4.7), treating the mass flow rates as inputs. In this model, the output temperatures

in  $\mathbf{y}$  are computed analogously to Eq. 4.29. The discrete-time linearization of this observer submodel is represented by matrices  $A_e$ ,  $B_e$ ,  $C_e$  and vectors  $\mathbf{x}'_e$ ,  $\mathbf{u}'_e$ ,  $\mathbf{f}_{0,e}$  and  $\mathbf{g}_{0,e}$  which are computed analogously to those used for control (see Sec. 5.2).

We use an extended Kalman filter (EKF) [Gelb, 1974] to compute the state estimate  $\hat{\mathbf{x}}$  from the measurements  $\mathbf{y}$ . Due to the approximations and coarser discretization used in the control model, there is significant mismatch between the control and simulation models. To achieve offset-free reference tracking under this plant-model mismatch, we augment the control model with an output disturbance  $\mathbf{d} \in \mathbb{R}^{l_y}$  acting on each measurement [Maeder et al., 2009]. A similar approach would be required for a real plant, where the true behaviour can never be modelled exactly.

The dynamics and outputs of this augmented system are [Maeder et al., 2009]

$$\begin{bmatrix} \mathbf{x}'_{e,k+1} \\ \mathbf{d}_{k+1} \end{bmatrix} = \begin{bmatrix} A_e & 0 \\ 0 & I \end{bmatrix} \begin{bmatrix} \mathbf{x}'_{e,k} \\ \mathbf{d}_k \end{bmatrix} + \begin{bmatrix} B_e \\ 0 \end{bmatrix} \mathbf{u}'_{e,k} + \begin{bmatrix} \mathbf{f}_{0,e} \\ 0 \end{bmatrix} \quad (5.9)$$

and

$$\mathbf{y}_k = [C_y \quad I] \begin{bmatrix} \mathbf{x}'_{e,k} \\ \mathbf{d} \end{bmatrix} + \mathbf{g}_{0,e}. \quad (5.10)$$

Defining the augmented state vector  $\chi_k = [\mathbf{x}'_{e,k} \quad \mathbf{d}_k]^\top$ , we write the model given by Eqs. 5.9 and 5.10 as

$$\begin{aligned} \chi_{k+1} &= A_a \chi_k + B_a \mathbf{u}'_k + \mathbf{f}_{0,a} \\ \mathbf{y}_k &= C_a \chi_k + \mathbf{g}_{0,e}. \end{aligned} \quad (5.11)$$

The EKF assumes that the augmented system dynamics are given by

$$\begin{aligned} \chi_{k+1} &= F(\chi_k, \mathbf{u}'_k) + \mathbf{w}_k \\ \mathbf{y}_k &= G(\chi_k, \mathbf{u}'_k) + \mathbf{v}_k, \end{aligned} \quad (5.12)$$

where  $F$  and  $G$  represent the dynamics and output models in Equation 5.11, and  $\mathbf{w}_k$  and  $\mathbf{v}_k$  are zero-mean white noise processes with covariance matrices  $\Sigma_w \in \mathbb{R}^{n+l_y \times n+l_y}$  and  $\Sigma_v \in \mathbb{R}^{l_y \times l_y}$  respectively. Furthermore, it assumes that at timestep  $k$ , the state estimate  $\hat{\chi}_k$  is a normally-distributed random variable with mean  $\bar{\chi}_k$  and covariance  $\Sigma_{x,k} \in \mathbb{R}^{n \times n}$ . We denote the mean of the output estimate corresponding to  $\hat{\chi}_k$  as  $\bar{\mathbf{y}}_k$ .

We update the state estimate by first computing the predicted next-timestep state and output estimates as

$$\begin{aligned} \bar{\chi}_k^\dagger &= F(\bar{\chi}_{k-1}, \bar{\mathbf{u}}_{k-1}) \\ \bar{\mathbf{y}}_k^\dagger &= G(\bar{\chi}_k^\dagger) \\ \Sigma_{x,k}^\dagger &= A_a \Sigma_{x,k-1} A_a^\top + \Sigma_w. \end{aligned} \quad (5.13)$$

Then, using the measurements  $\mathbf{y}_k$ , we correct the state estimate according to

$$\begin{aligned} \mathbf{i}_k &= \mathbf{y}_k - \bar{\mathbf{y}}_k^\dagger \\ K_k &= \Sigma_{x,k}^\dagger C_a^\top \left( C_a \Sigma_{x,k}^\dagger C_a^\top + \Sigma_v \right)^{-1} \\ \bar{\chi}_k &= \bar{\chi}_k^\dagger + K_k \mathbf{i}_k \\ \Sigma_{x,k} &= (I - K_k C_a) \Sigma_{x,k}^\dagger (I - K_k C_a)^\top + K_k \Sigma_{v,k} K_k^\top, \end{aligned} \quad (5.14)$$

where  $\mathbf{i}_k$  is the innovation and  $K_k$  is the Kalman gain.

We set values for the noise covariance matrices based on nominal values for the estimated states and outputs ( $T_{CO_2,nom}$ ,  $e_{CO_2,nom}$ ,  $T_{oil,nom}$ ,  $e_{oil,nom}$  and  $T_{wall,nom}$  — see Tab. 2 for values). We assume that all measurements are independent and that measurement error is normally distributed with zero mean and variance of 2% of the nominal measured value. Thus, the measurement noise covariance is

$$\Sigma_v = 0.02 \times \text{diag} (T_{CO_2,nom} \quad T_{CO_2,nom} \quad T_{oil,nom} \quad T_{oil,nom}). \quad (5.15)$$

We assume that the continuous-time process noise  $\Sigma_{w,c}$  is diagonal with a power spectral density of one. Additionally, we assume that variance of the state variables ( $\mathbf{e}_{hot}$ ,  $\mathbf{e}_{cold}$ , and  $\mathbf{T}_{wall}$ ) is 10% of nominal and that the variance of the disturbances variables is 5% of nominal. Under these assumptions, the continuous-time process noise is

$$\begin{aligned} \Sigma_{w,c} &= \text{diag} (0.1 \mathbf{T}_{wall,nom} \quad 0.1 \mathbf{e}_{CO_2,nom} \quad 0.1 \mathbf{e}_{oil,nom} \\ &0.05 T_{CO_2,nom} \quad 0.05 T_{CO_2,nom} \quad 0.05 T_{oil,nom} \quad 0.05 T_{oil,nom}), \end{aligned} \quad (5.16)$$



where  $\mathbf{e}_{CO_2, nom}$  is a vector of length  $N_{cells}$  ( $\mathbf{e}_{CO_2, nom} = [e_{CO_2, nom}, \dots, e_{CO_2, nom}]$ ) and similar for  $\mathbf{e}_{cold, nom}$  and  $\mathbf{T}_{wall, nom}$ . Using the most recent augmented LTI model, we approximate the discrete-time process noise as

$$\Sigma_w = A_a \Sigma_{w,c} A_a^T \Delta t. \quad (5.17)$$

Our state estimation approach accounts for model mismatch in the models of the fluid streams, but not in the turbo-machinery performance maps. This approach is reasonable, since for a real plant, the performance maps could be frequently updated based on real operating data, removing mismatch. If accurate performance maps were not used, the observer would need to also estimate output power (with an associated disturbance) to achieve offset-free tracking.

Table 2: Nominal variable values for estimator tuning

Variable	Value
$p_{oil, nom}$ :	4.0 MPa
$T_{oil, nom}$ :	570 K
$e_{oil, nom}$ :	EOS( $p_{oil, nom}, T_{oil, nom}$ )
$p_{CO_2, nom}$ :	12.0 MPa
$T_{CO_2, nom}$ :	520 K
$e_{CO_2, nom}$ :	EOS( $p_{CO_2, nom}, T_{CO_2, nom}$ )

## 5.4 MPC formulation

Here, we develop a model predictive controller for the control problem presented in Sec. 2. We use tracking MPC [Maciejowski, 2002] with the estimator detailed in Sec. 5.3. We compute the tracked outputs as

$$\mathbf{z}_k = C_z \mathbf{x}'_k + C_d \mathbf{d}_k + \mathbf{g}_0 \quad (5.18)$$

where the matrix  $C_d$  maps the disturbances on to the tracked outputs. Since  $T_{CO_2, out} = T_{in, t}$ ,

$$C_d = \begin{pmatrix} 0 & 0 & 0 & 0 \\ 0 & 1 & 0 & 0 \end{pmatrix}. \quad (5.19)$$

From the current reference vector  $\mathbf{r}_k$ , we compute the target state  $\mathbf{x}'_r$  and input  $\mathbf{u}'_r$  by solving the continuous-time system

$$\begin{bmatrix} A & B \\ C_z & 0 \end{bmatrix} \begin{bmatrix} \mathbf{x}'_r \\ \mathbf{u}'_r \end{bmatrix} = \begin{bmatrix} -\mathbf{f}_0 \\ \mathbf{r}_k - C_d \hat{\mathbf{d}}_k - \mathbf{g}_0 \end{bmatrix} \quad (5.20)$$

for the current disturbance estimate  $\hat{\mathbf{d}}_k$  (see Sec. 5.3). We use tracking MPC with a terminal state cost and costs on control moves, so the cost functional takes the form [Maciejowski, 2002]

$$J(k, \mathbf{x}_k, \mathbf{U}) = \left\| \mathbf{x}'_{k+H_p} - \mathbf{x}'_r \right\|_P^2 + \sum_{i=0}^{H_p-1} \left\| \mathbf{x}'_{k+i} - \mathbf{x}'_r \right\|_Q^2 + \left\| \Delta \mathbf{u}_{k+i} \right\|_R^2, \quad (5.21)$$

where  $H_p$  is the prediction horizon,  $\mathbf{U}$  is the vector of control inputs

$$\mathbf{U} = \left[ \mathbf{u}'_k, \mathbf{u}'_{k+1}, \dots, \mathbf{u}'_{k+H_p-1} \right]^T, \quad (5.22)$$

$\Delta \mathbf{u}_{k+i} = \mathbf{u}'_{k+i} - \mathbf{u}'_{k+i-1}$ , and  $Q$ ,  $P$ , and  $R$  are stage, terminal, and input costs. We compute the stage cost from the output cost  $Q_z \in \mathbb{R}^{l \times l}$  as  $Q = C_z^T Q_z C_z$ , so that

$$\left\| \mathbf{x}' - \mathbf{x}'_r \right\|_Q^2 \equiv \left\| \mathbf{z} - \mathbf{r} \right\|_{Q_z}^2. \quad (5.23)$$

As the plant is open-loop stable, we can obtain a stable control law by computing the terminal cost as the solution of the discrete-time matrix Lyapunov equation [Maciejowski, 2002]

$$A_d^T P A_d - P + Q = 0. \quad (5.24)$$

At each  $k$ , to compute the next control update  $\mathbf{u}_k$ , we solve the constrained QP

$$\begin{aligned} \min_{\mathbf{U}} \quad & J(k, \mathbf{x}_k, \mathbf{U}) \\ \text{subject to} \quad & \mathbf{x}'_{k+i+1} = A_d \mathbf{x}'_{k+i} + B_d \mathbf{u}'_{k+i} + \mathbf{f}_{0,d} \\ & \text{for } i = 1, \dots, H_p - 1 \\ & \mathbf{z} \in \mathcal{Z} \\ & \mathbf{u} \in \mathcal{U} \end{aligned} \quad (5.25)$$

for the current augmented state estimate  $(\hat{\mathbf{x}}_k, \hat{\mathbf{d}}_k)$  and previous control input  $\mathbf{u}_{k-1}$ .  $\mathcal{U}$  and  $\mathcal{Z}$  represent the admissible input and output sets, which are discussed in Sec. 5.5. Our model has a relatively high state dimensionality due to the discretization of the fluid streams. Thus, we formulate the QP using dense matrices (as in Maciejowski [2002]), so its computational complexity depends only on  $m$  and  $l$  (and not  $n$ ) [Wang and Boyd, 2010]. We solve the QPs using Gurobi [Gurobi Optimization, 2018]. Using slack variables, we implement the constraints on  $\mathbf{z}$  as soft constraints with weightings discussed in Sec. 5.5. The constraint weights are set such that constraint violations are negligible for all tested cases.

## 5.5 Constraints

In addition to the compressor speed constraints (see Sec. 4.6), we also consider input constraints and a maximum turbine inlet temperature constraint. To guarantee feasibility of the optimization problems, state and output constraints are implemented as soft constraints using weighted linear penalization (see Tab. 3 for parameter values). Constraint weights were set such that state and output constraint violations are negligible.

Table 3: Constraint bounds and soft constraint parameters

Variable	Constraint	Weight
Compressor speed:	See Sec. 4.6	1E6
Turbine inlet temperature:	$T_{in,t} \leq 570$ K	2000
Motor torque:	$0 \leq T_{motor} \leq 200$ Nm	-
	$-15 \leq \dot{T}_{motor} \leq 15$ Nm/s	-
Heat transfer oil flow rate:	$3 \leq \dot{m}_{oil} \leq 25$ kg/s	-
	$-1.2 \leq \ddot{m}_{oil} \leq 1.2$ kg/s <sup>2</sup>	-

## 6 Results and discussion

This section presents the results of closed-loop simulations of the open sCO<sub>2</sub> cycle detailed in Sec. 2 according to the approach shown in Fig. 3. These simulations use the simulation model, control model, and controller presented in Secs. 3, 5, and 4 respectively.

### 6.1 Controller tuning

The controller was manually tuned on the test cases presented in Sec. 6.2, yielding the weights in Eq. 6.1 and parameter values in Tab. 4. The controller was tuned according to the following logic. Plants that can respond quickly to power demand changes are critical for maintaining power quality and reliability, especially with high supply-side uncertainty, so net power tracking is weighted highly. Turbine inlet temperature tracking corresponds to maximizing cycle thermodynamic efficiency, which brings moderate financial benefit, but does not affect power system stability, and so thus weighted less highly. The control input weights were tuned to (1) give smooth closed-loop response and (2) prioritize the use of compressor torque for net power tracking, due to its predictable and controllable dynamics. (Due to the typical ranges of each tracked output, the absolute value of the turbine inlet temperature tracking weight is larger than that for net power.)

$$\begin{aligned} \text{diag}(Q_z) &= [1\text{E}-3, 2\text{E}1] & \left( \mathbf{z} = [\dot{W}_{net}, T_{in,t}] \right) \\ \text{diag}(R) &= [2\text{E}2, 1\text{E}5] & \left( \mathbf{u} = [\dot{T}_m, \ddot{m}_{oil}] \right) \end{aligned} \quad (6.1)$$

The sampling time, prediction horizon, and control model fidelity (set by the level of discretization in the fluid streams) were set such that (1) the controller can adequately control the fastest system dynamics, (2) the prediction horizon covers a large portion of a typical transient, and (3) the controller is computationally tractable. For the chosen settings, control updates are reliably computed in less than 0.03 s (10% of the sampling time) using a 2015 Intel® Core™ i7-4770.

### 6.2 Closed-loop simulations

This section evaluates the controller's performance through closed-loop simulations. In these simulations, for each target power output  $\dot{W}_{net,ref}$ , the turbine inlet temperature setpoint  $T_{in,t,ref}$  is set as the maximum steady-state turbine inlet temperature, as dictated by system constraints (see Sec. 5.5).

Table 4: Controller settings

Parameter	Value
Sampling time $\Delta t$ :	0.3 s
Estimator sampling time $\Delta t_e$ :	0.06 s
Prediction horizon $H_p$ :	30 steps (9 s)
Heat exchanger cells (control model) $N_{cells, HX}$ :	15 cells
Pipe cells (control model) $N_{cells, pipes}$ :	5 cells
MPC weighting matrices $Q, P, R$ :	See Eq. 6.1

The first set of simulations (Fig. 8a) show closed-loop performance near the design-point power output. In this region, the system can achieve the target net power outputs at the design-point turbine inlet temperature of 565 K. The core system dynamics are weakly coupled near the design point as the controller can quickly manipulate compressor torque to enact output power changes, while more gradually manipulating thermal oil flow rate to track turbine inlet temperature.

Near the design-point (Fig. 8a), the controller tracks net power output setpoints quickly, with no steady-state error, and with negligible overshoots. The controller enacts fast load changes by aggressively manipulating compressor torque. For example, in response to the load reduction, the controller first decreases compressor torque at its rate constraint then quickly increases it again to quickly attain the new target power output without overshooting. The controller also tracks turbine inlet temperature setpoints well, but less tightly than for net power, as expected due to its tuning (see Sec. 6.1) and the slower dynamics of temperatures (compared to mass flow rates). The controller maintains turbine inlet temperature within 10 K of the design value despite operating between approximately 60 to 105% of nominal power output. The compressor surge and turbine inlet temperature constraints are handled well, with virtually no violations of either. Closed-loop performance is similar over the entire tested operating range.

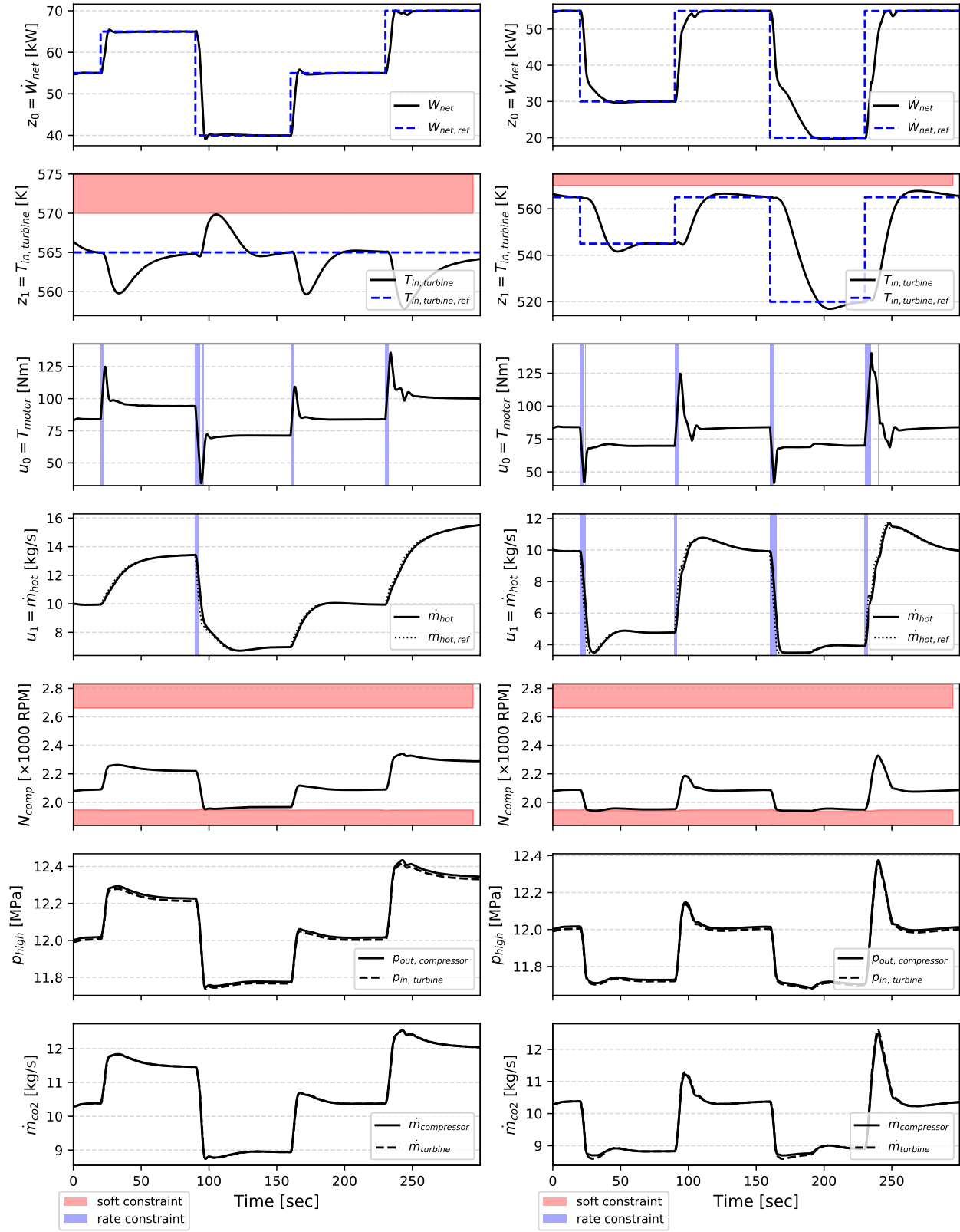
The second set of simulations (see Fig. 8b) show highly off-design operation, with target power outputs far below the nominal value. To reach low power outputs (below 60% of nominal) without violating the surge constraint, the turbine inlet temperature target must be reduced below its design value. Varying the turbine inlet temperature target makes control challenging for the following reasons: (1) thermal transients are highly nonlinear and are coupled with CO<sub>2</sub> mass flow (see Sec. 4.4); (2) the compressor operates at the surge boundary for extended periods, limiting possible control actions; and (3) the turbine operates over more of its performance map.

For the off-design case (Fig. 8b), the controller still performs well, despite the wide and nonlinear range of operating points covered. Load increases are fast, with average ramp rates during transients comparable to those achieved near the design point (often in excess of 100% of nominal output per minute). Load reductions take longer as they are limited by the surge constraint. To significantly reduce net power output, the controller must reduce turbine inlet temperature to near its new (lower) target value, involving the fundamentally slower thermal dynamics of the fluid and component walls. For all load changes, the controller handles interactions between the thermal and mass flow transients well, and can deeply converge net power output (the most important variable operationally) to its target before converging turbine inlet temperature. Again, constraint satisfaction is excellent.

The results shown in Figs. 8a and 8b support the validity of the approximations used in the control model, particularly the quasi-steady momentum assumption. For the open sCO<sub>2</sub> cycle, this assumption has two implications: (1) High-side pressure varies instantaneously with turbine operating point (see Eq. 4.27). (2) Turbine mass flow rate generally follows compressor mass flow rate according to a first-order lag model, but deviates during strong thermal transients to account for the changing specific volume of CO<sub>2</sub> (see Eq. 4.28). The results for both design-point and off-design operation clearly follow these trends. Moreover, even during strong thermal transients, compressor and turbine mass flow rates are very close, suggesting that they may be modeled using a single variable in the control model. However, this approach does not provide a mechanism to model mass transfer between the high- and low-pressure sides of the system, which may be important when extending the proposed control strategy to closed cycles.

### 6.3 Discussion

Control of sCO<sub>2</sub> cycles is challenging due to their complex dynamics, which arise from non-ideal-gas effects and their non-condensing design. Existing model-based control strategies for similar systems (such as gas turbines) are not applicable to sCO<sub>2</sub> cycles as they do not consider non-ideal-gas effects. This article develops a control model for sCO<sub>2</sub> cycles by applying timescale-separation techniques to a high-fidelity truth model, and by locally linearizing non-ideal-gas turbomachinery performance maps. This model is theoretically accurate over a wide operating range, subject to validity of the heat transfer correlations and performance maps.



(a) Closed-loop simulation, operation near design-point

(b) Closed-loop simulation, highly off-design operation

Figure 8: Closed-loop simulations

Overall, the controller performs well for all test cases supporting the validity of the proposed control strategy. For MPC, the quality of control depends strongly on the accuracy of the control model, suggesting that the low-order control model (Sec. 4) approximates the dynamics of the high-fidelity simulation model (Sec. 3) reasonably well. With some modifications — namely, relaxing the fixed low-side pressure assumption and adding a valve model — the control model could be used to implement MPC for more realistic sCO<sub>2</sub> cycle variants, such as the recuperated cycle or recompression cycle. The proposed modelling approach may also be applied to similar non-condensing non-ideal-gas power cycles.

MPC is implemented by linearizing the nonlinear control model online at each sampling instant. For this system, obtaining good performance from linear MPC requires that we retain only certain terms in the linearizations of the wall temperature and stream internal energy models (see Eqs. 4.4 and 4.8). With this approach, good performance is obtained using linear MPC, even for large setpoint changes that cover a wide nonlinear operating range. With linear MPC, the control updates are computed reliably and quickly — in less than 10% of sampling interval on a 2015 Intel® Core™ i7-4770. It is unclear if linear MPC will still be suitable when considering more complex cycle configurations with variable low-side pressure and recuperation, however the our control modelling approach is equally compatible with nonlinear MPC solvers.

The load changes demonstrated in this article are fast for a thermal power plant. During design-point and off-design load changes, the controller demonstrates average ramp rates of approximately 150% of nominal power output per minute. There are two caveats to this result: the system is small-scale, and is simpler than a recuperated or recompression sCO<sub>2</sub> cycle, which removes some challenging dynamics associated with recuperation and variable low-side pressure. Real plants may also face additional constraints, such as maximum thermal ramp rates in component walls or casings. Slower load changes are expected for more complex cycle configurations and for real plants, but the encouraging results presented in this article justify further investigation into the application of MPC to the sCO<sub>2</sub> cycle or related power cycles.

The results presented herein demonstrate several of MPC’s principal strengths. For example, the controller responds rapidly to setpoint changes, coordinating both control inputs to enact fast and precise changes in net power output. Despite the system’s highly nonlinear dynamics, the controller performs well over a very wide operating range, covering 35 to 105% of nominal power output, without any scheduling of tuning parameters. The results also highlight MPC’s constraint handling capabilities, with the controller acting on input constraints in response to strong transients and reliably preventing state constraints from being violated. The controller can safely track turbine inlet temperature setpoints that lie close to the maximum turbine inlet temperature, and can reliably operate close to the compressor surge boundary, thus expanding the safe operating range of the system. Many of these qualities directly impact the ‘flexibility’ of the system, allowing it more quickly respond to load changes and function over a wider and more efficient operating envelope. These benefits would likely apply to other non-ideal-gas cycles, suggesting that MPC might be a useful tool for improving the flexibility of thermal power plants more generally, thus facilitating higher renewable penetration.

## 7 Conclusion

This article presented a methodology to implement MPC for non-condensing non-ideal-gas power cycles, then tested this methodology on the high-pressure side of simple sCO<sub>2</sub> cycle power block. First, to faithfully replicate the system’s dynamics, we presented a high-fidelity gas-dynamics simulation model integrated with empirical non-ideal-gas turbomachinery submodels. Next, we developed a control model by applying timescale separation arguments to the simulation model, then implemented MPC via online relinearization of this control model. Finally, we performed closed-loop simulations of a laboratory-scale sCO<sub>2</sub> cycle using the high-fidelity simulation model as a substitute for the real plant. These simulations demonstrated the effectiveness of the proposed controller for tracking output power setpoint changes while keeping the system at target turbine inlet temperatures. The simulations show that MPC’s core strengths, such as good dynamic performance over a wide operating range and routine handling of constraints, increase the plant’s achievable ramp rates and expand its safe operating envelope. These flexibility improvements likely apply to other thermal power plants, suggesting that MPC might be useful for improving power system flexibility more generally, thus facilitating higher renewable energy share. The controller is computationally tractable on a standard computer, and with some modifications, may be extended to more realistic sCO<sub>2</sub> cycle configurations.

## A Performance map models

This appendix describes the turbomachinery performance map models used in this work. These models are used to compute  $\dot{m}_{tb}$  and  $T_{out}$  for a turbomachine given  $p_{in}$ ,  $p_{out}$ ,  $T_{in}$ , and  $N_s$  (as per Eq. 3.11). We focus on radial inflow

turbines and centrifugal compressors, which are appropriate for smaller output power sCO<sub>2</sub> cycles, such as remote or modular plants [Jahn and Keep, 2017]. Our approach is equally applicable to axial turbomachinery provided that appropriate maps are used.

### A.1 Turbine

For typical sCO<sub>2</sub> cycle operating conditions, the turbine operates in CO<sub>2</sub>'s ideal-gas-like region, so ideal-gas scaling relations can be used to model off-design turbine operation [Jahn and Keep, 2017]. Under this approach [Glassman, 1972, Whitfield and Baines, 1990], turbine performance is parametrized using the mass flow parameter

$$\text{MFP} = \dot{m}_{tb} \sqrt{T_{in}} / p_{in} \quad (\text{A.1})$$

and corrected speed

$$N_{cor} = N_s \sqrt{T_{in} / T_{in, des}}, \quad (\text{A.2})$$

where  $T_{in, des}$  is the design-point inlet temperature.

The design-point performance of a radial inflow turbine operating in the ideal gas region can be characterized by two maps [Glassman, 1972, Whitfield and Baines, 1990] (shown in Fig. 9):

$$\text{MFP} = M_{t1}(\text{PR}, N_{cor}) \quad (\text{A.3})$$

$$\eta = M_{t2}(v_{tip}/v_{is}), \quad (\text{A.4})$$

where the pressure ratio is  $\text{PR} = p_{in}/p_{out}$  and  $v_{tip}/v_{is}$  is the ratio of turbine tip speed to the isentropic spouting velocity of the gas (these two variables lie on the x-axes of the maps).

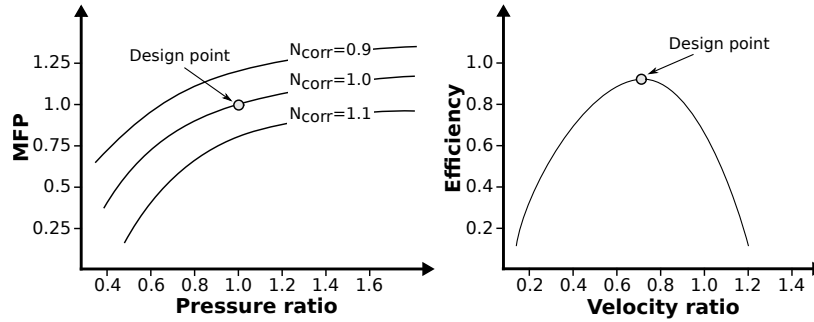


Figure 9: Sample turbine performance maps [Glassman, 1972, Whitfield and Baines, 1990]

The turbine performance maps are evaluated as follows. First, we compute MFP from PR using the map  $M_{t1}$  and  $N_{cor}$ , then we compute  $\dot{m}_{tb}$  from Eq. A.1. Next, we compute the isentropic spouting velocity for the current operating point as

$$v_{is} = \sqrt{2 C_{p, in} T_{in} \left(1 - \text{PR}^{\gamma_{in}/(\gamma_{in}-1)}\right)}, \quad (\text{A.5})$$

where the constant pressure and constant volume specific heats are computed from the inlet state and the ratio of specific heats is  $\gamma_{in} = C_{p, in}/C_{v, in}$ . We then re-evaluate Eq. A.5 using the design-point pressure ratio and inlet temperature to get the design-point isentropic spouting velocity  $v_{is, des}$ . Next, we compute the velocity ratio as

$$v_{tip}/v_{is} = (v_{tip}/v_{is})_{des} (N_{cor}/N_{des}) (v_{is}/v_{is, des}). \quad (\text{A.6})$$

From  $v_{tip}/v_{is}$ , we compute  $\eta$  from map  $M_{t2}$  then solve for the outlet state using

$$\eta = (h_{in} - h_{out}) / (h_{in} - h_{out, is}). \quad (\text{A.7})$$

The remaining outlet properties are then computed using the equation of state.

In this work, the turbine performance maps are based on data from Hiatt and Johnston [1963], who published geometries and performance maps for a range of radial inflow gas turbines developed by Ricardo & Co. We use the data for the A70 turbine design due to its geometric similarity to power generation turbines and similarity in pressure ratio and stage-Mach number to the turbines employed for sCO<sub>2</sub> cycles.

## A.2 Compressor

In the sCO<sub>2</sub> cycle, the compressor inlet conditions are typically close to CO<sub>2</sub>'s critical point, where the fluid properties enable efficient compression. However, the strong non-ideal-gas property variations in this region cause compressor performance to change substantially when operating at off-design inlet conditions. To capture these non-ideal-gas scaling effects, we use 2D compressor maps that are parametrized using the corrected variables  $\dot{m}_{cor}$ ,  $N_{cor}$ , and  $\Delta h_{cor}$  [Glassman, 1972]. These corrected variables are computed based on the deviation of the inlet conditions from some chosen standard conditions ( $p_{std}$ ,  $T_{std}$ ), which for sCO<sub>2</sub> cycles are chosen as CO<sub>2</sub>'s critical point (7.366 MPa and 304.1 K). From the standard conditions, the corrected variables are [Glassman, 1972]

$$\dot{m}_{cor} = \dot{m}_{tb} \sqrt{1/V_{cr}} (p_{std}/p_{in}) \epsilon \quad (\text{A.8})$$

$$N_{cor} = N_s V_{cr} \quad (\text{A.9})$$

$$\Delta h_{cor} = \Delta h V_{cr} \quad (\text{A.10})$$

where the non-ideal-gas scaling factors  $V_{cr}$  and  $\epsilon$  are

$$V_{cr} = (\gamma_{in, std} (\gamma_{in} + 1) T_{std}) / (\gamma_{in} (\gamma_{in, std} + 1) T_{in}) \quad (\text{A.11})$$

$$\epsilon = \left( \left( \frac{2\gamma_{in, std}}{\gamma_{in, std} + 1} \right)^{(1-\gamma_{in, std}^{-1})^{-1}} \right) / \left( \frac{2\gamma_{in}}{\gamma_{in} + 1} \right)^{(1-\gamma_{in}^{-1})^{-1}} \quad (\text{A.12})$$

Using these corrected variables, compressor performance can be characterized using two 2D maps (shown in Fig. 10):

$$\Delta h_{cor} = M_{c1}(\dot{m}_{cor}, N_{cor}) \quad (\text{A.13})$$

$$\eta = M_{c2}(\dot{m}_{cor}, \Delta h_{cor}). \quad (\text{A.14})$$

The compressor maps are evaluated in forward mode (where  $T_{out}$  and  $p_{out}$  are outputs — see Eq. 3.9), as follows. First,  $\dot{m}_{tb, cor}$  and  $N_{cor}$  are computed from the compressor inlet conditions with Eqs. A.8 and A.9. Then,  $\Delta h_{cor}$  and  $\eta$  are computed from the maps  $M_{c1}$  and  $M_{c2}$ . Finally,  $\Delta h$  is computed using Eq. A.10, then the outlet state is computed from  $\eta$  using Eq. A.7 (as done for the turbine).

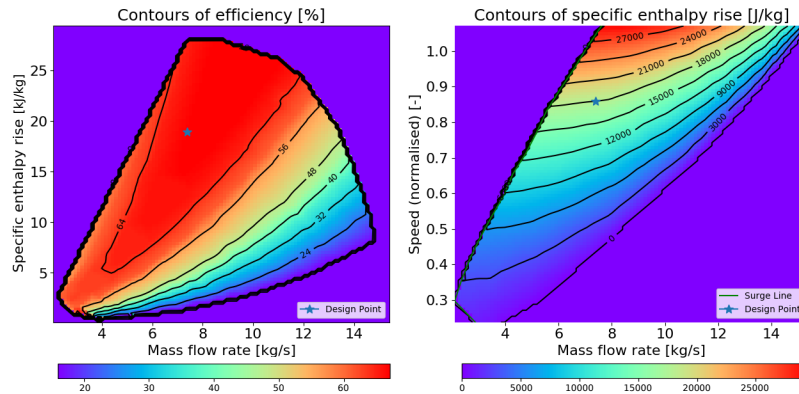


Figure 10: Design-point compressor performance maps [Jahn and Keep, 2017]. Off-design performance can be modeled by evaluating the maps with corrected variables  $\dot{m}_{tb, cor}$ ,  $N_{cor}$ , and  $\Delta h_{cor}$ .

### Evaluation of compressor model from pressure ratio

The compressor performance map model cannot be explicitly reformulated in terms of pressure ratio. Accordingly, in simulations, we evaluate this model from inputs  $p_{in}$ ,  $p_{out}$ ,  $T_{in}$ , and  $N_s$  (see Eq. 3.11) by solving the following root-finding problem (illustrated in Fig. 11):

$$\begin{aligned} \hat{p}_{out}, \hat{T}_{out} &= f_{tb}(\hat{m}_{tb}, p_{in}, T_{in}, N_s) \\ 0 &= p_{out} - \hat{p}_{out}. \end{aligned} \quad (\text{A.15})$$

In other words, we compute the compressor mass flow  $\hat{m}_{tb}$  such that  $f_{tb}$  gives the correct  $p_{out}$ , then take the outlet fluid state as  $(p_{out}, \hat{T}_{out})$ .

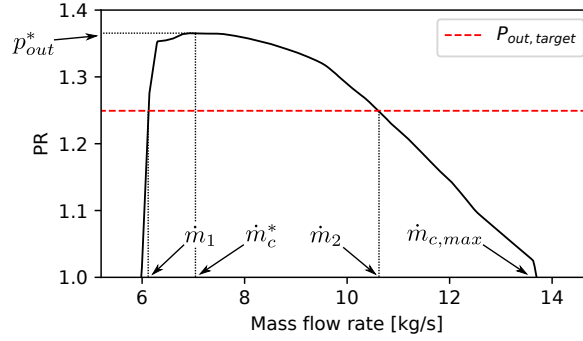


Figure 11: Compressor PR versus mass flow curve for  $N_s = 0.916$ ,  $T_{in} = 320$  K, and  $p_{in} = 8.629$  MPa. The target outlet pressure is 12.5 MPa.

As shown in Fig. 11, there are two solutions to this root-finding problem ( $\dot{m}_1$  and  $\dot{m}_2$ ). Due to the surge control that we employ (see Sec. 4.6), the compressor is maintained at the right-side solution  $\dot{m}_2$ . We ensure that the root-finder finds this solution by imposing bounds

$$\dot{m}_c^* \leq \hat{m}_{tb} \leq \dot{m}_{c, max}, \quad (\text{A.16})$$

where the surge and maximum mass flow rates are evaluated from lookup tables as

$$\begin{aligned} \dot{m}_c^* &= f_{c2}(N_{cor}) \\ \dot{m}_{c, max} &= f_{c3}(N_{cor}). \end{aligned} \quad (\text{A.17})$$

These lookup tables are formed from data used to build the compressor maps.

We form the compressor maps using data from Clementoni et al. [2015]. These maps are linearly scaled by design-point mass flow rate and enthalpy rise to achieve the power output and pressure ratio. As primary performance factors (stage Mach number and pressure ratio) can be maintained through appropriate geometry selections, the scaled maps are representative of a real machine's behavior.

## References

- Paratherm HE thermal properties. <https://thermalprops.paratherm.com/HE.asp>. Accessed: 2020-10-23.
- Innovation landscape brief: Flexibility in conventional power plants. Technical report, International Renewable Energy Agency (IRENA), 2019.
- C Aurora, Moritz Diehl, P Kuehl, L Magni, and Riccardo Scattolini. Nonlinear model predictive control of combined cycle power plants. *IFAC Proceedings Volumes*, 38(1):127–132, 2005.
- Ian H. Bell, Jorrit Wronski, Sylvain Quoilin, and Vincent Lemort. Pure and pseudo-pure fluid thermophysical property evaluation and the open-source thermophysical property library coolprop. *Industrial & Engineering Chemistry Research*, 53(6):2498–2508, 2014. doi: 10.1021/ie4033999. URL <http://pubs.acs.org/doi/abs/10.1021/ie4033999>.
- Viv Bone, Rob McNaughton, Michael Kearney, and Ingo Jahn. Methodology to develop off-design models of heat exchangers with non-ideal fluids. *Applied Thermal Engineering*, 2018.
- Viv Bone, Thomas Reddell, Michael Kearney, and Ingo Jahn. Output-feedback model predictive control of non-ideal-gas heat exchangers. In *Proceedings of GPPS Beijing, 2019*. Global Power & Propulsion Society, 2019.
- Nathan Carstens. *Control strategies for supercritical carbon dioxide power conversion systems*. PhD thesis, Massachusetts Institute of Technology, 2007.
- Jeff R Cash and Alan H Karp. A variable order Runge-Kutta method for initial value problems with rapidly varying right-hand sides. *ACM Transactions on Mathematical Software (TOMS)*, 16(3):201–222, 1990.
- Eric M Clementoni, Timothy L Cox, and Martha A King. Off-nominal component performance in a supercritical carbon dioxide brayton cycle. In *Turbo Expo: Power for Land, Sea, and Air*, volume 56802, page V009T36A002. American Society of Mechanical Engineers, 2015.



- Richard Courant, Kurt Friedrichs, and Hans Lewy. On the partial difference equations of mathematical physics. *IBM journal of Research and Development*, 11(2):215–234, 1967.
- Fernando Javier D’Amato. Industrial application of a model predictive control solution for power plant startups. In *2006 IEEE International Conference on Control Applications*, pages 243–248. IEEE, 2006.
- Vaclav Dostal. *A supercritical carbon dioxide cycle for next generation nuclear reactors*. PhD thesis, Massachusetts Institute of Technology, Department of Nuclear Engineering, 2004.
- Sanjeev Duggal, Mahesh Kendhe, and R. Sanyaswara Ganti. Techno-economic assessment of integrating 175GW of renewable energy into the Indian grid by 2022. Technical report, General Electric (GE), 2017.
- F D’Amato, A Kumar, R Lopez-Negrete, and LT Biegler. Fast nonlinear model predictive control: Optimization strategy and industrial process applications. In *Proc. of the chemical process control conference VIII conference. GA: Savannah Harbor*, 2012.
- Agora Energiewende. Flexibility in thermal power plants. Technical report, 2017.
- Amir Faghri, Yuwen Zhang, and John R Howell. *Advanced heat and mass transfer*. Global Digital Press, 2010.
- Andreas Feldmüller. Flexibility of coal and gasfired power plants, 2018. Advanced Power Plant Flexibility Campaign, Paris.
- A Fenghour, William A Wakeham, and V Vesovic. The viscosity of carbon dioxide. *Journal of Physical and Chemical Reference Data*, 27(1):31–44, 1998.
- Gene F Franklin, J David Powell, and Michael L Workman. *Digital control of dynamic systems*, chapter 2. Addison-Wesley Reading, MA, 1990.
- Arthur Gelb. *Applied optimal estimation*. MIT press, 1974.
- Arthur J Glassman. Turbine design and application. NASA special report 290, National Aeronautics and Space Administration (NASA), 1972.
- Jan Tommy Gravdahl and Olav Egeland. *Compressor surge and rotating stall: Modeling and control*. Springer Science & Business Media, 2012.
- LLC Gurobi Optimization. Gurobi optimizer reference manual, 2018. URL <http://www.gurobi.com>.
- GF Hiett and IH Johnston. Paper 7: Experiments concerning the aerodynamic performance of inward flow radial turbines. In *Proceedings of the institution of mechanical engineers, conference proceedings*, volume 178, pages 28–42. SAGE Publications Sage UK: London, England, 1963.
- Nicholas J Higham. The scaling and squaring method for the matrix exponential revisited. *SIAM Journal on Matrix Analysis and Applications*, 26(4):1179–1193, 2005.
- International Energy Agency (IEA). Status of power system transformation. Technical report, 2019.
- Raad I Issa. Solution of the implicitly discretised fluid flow equations by operator-splitting. *Journal of computational physics*, 62(1):40–65, 1986.
- Peter A. Jacobs and Rowan J. Gollan. The Eilmer 4.0 flow simulation program: Guide to the transient flow solver, including some examples to get you started. School of Mechanical and Mining Engineering Technical Report 2017/26, The University of Queensland, Brisbane, Australia, February 2018.
- Ingo HJ Jahn and Joshua A Keep. On the off-design performance of supercritical carbon dioxide power cycles. In *Proceedings of GPPS Shanghai, 2017*. Global Power & Propulsion Society, 2017.
- J Kassakian, R Schmalensee, G Desgroseilliers, T Heidel, K Afridi, A Farid, J Grochow, W Hogan, H Jacoby, J Kirtley, et al. *The Future of the Electric Grid: An Interdisciplinary MIT Study*. MIT Press, Cambridge, MA, 2011.
- Jong S Kim, Kody M Powell, and Thomas F Edgar. Nonlinear model predictive control for a heavy-duty gas turbine power plant. In *2013 American control conference*, pages 2952–2957. IEEE, 2013.
- Nikhil Kumar, P Besuner, S Lefton, D Agan, and D Hilleman. Power plant cycling costs. Technical report, National Renewable Energy Lab.(NREL), Golden, CO (United States), 2012.
- Xiaobing Liu, Adamu Yebi, Paul Ansel, John Shutt, Bin Xu, Mark Hoffman, and Simona Onori. Model predictive control of an organic rankine cycle system. *Energy Procedia*, 129:184–191, 2017.
- Jan Marian Maciejowski. *Predictive control: with constraints*. Pearson education, 2002.
- Urban Maeder, Francesco Borrelli, and Manfred Morari. Linear offset-free model predictive control. *Automatica*, 45(10):2214–2222, 2009.

- A Moisseytsev and JJ Sienicki. Development of a plant dynamics computer code for analysis of a supercritical carbon dioxide brayton cycle energy converter coupled to a natural circulation lead-cooled fast reactor. Technical report, Argonne National Laboratory (ANL), Argonne, IL, 2007.
- A Moisseytsev and JJ Sienicki. Development of the anl plant dynamics code and control strategies for the supercritical carbon dioxide brayton cycle and code validation with data from the sandia small-scale supercritical carbon dioxide brayton cycle test loop. Technical report, Argonne National Lab.(ANL), Argonne, IL (United States), 2011.
- A Moisseytsev and JJ Sienicki. Progress report on dynamic simulation of the sandia small-scale supercritical carbon dioxide brayton cycle test loop with the anl plant dynamics code. Technical report, Argonne National Lab.(ANL), Argonne, IL (United States), 2012.
- Anton Moisseytsev and James J Sienicki. Simulation of ist turbomachinery power-neutral tests with the anl plant dynamics code. Technical report, Argonne National Lab.(ANL), Argonne, IL (United States), 2016.
- G. Musgrove and S. Wright. Introduction and background. In K. Brun and R. Dennis, editors, *Fundamentals and Applications of Supercritical Carbon Dioxide (sCO<sub>2</sub>) Based Power Cycles*, Woodhead Publishing in energy, chapter 1, pages 1–21. Elsevier Science & Technology, 2017. ISBN 9780081008041.
- G. Musgrove, S. Sullivan, D. Shiferaw, P. Fourspring, and L. Chordia. Heat exchangers. In K. Brun and R. Dennis, editors, *Fundamentals and Applications of Supercritical Carbon Dioxide (sCO<sub>2</sub>) Based Power Cycles*, Woodhead Publishing in energy, chapter 8, pages 217–244. Elsevier Science & Technology, 2017. ISBN 9780081008041.
- Tri Lam Ngo, Yasuyoshi Kato, Konstantin Nikitin, and Takao Ishizuka. Heat transfer and pressure drop correlations of microchannel heat exchangers with s-shaped and zigzag fins for carbon dioxide cycles. *Experimental Thermal and Fluid Science*, 32(2):560–570, 2007.
- G Prasad, E Swidenbank, and BW Hogg. A local model networks based multivariable long-range predictive control strategy for thermal power plants. *Automatica*, 34(10):1185–1204, 1998.
- G Prasad, GW Irwin, E Swidenbank, and BW Hogg. Plant-wide predictive control for a thermal power plant based on a physical plant model. *IEE Proceedings-Control Theory and Applications*, 147(5):523–537, 2000.
- Dhruvang Rathod, Bin Xu, Zoran Filipi, and Mark Hoffman. An experimentally validated, energy focused, optimal control strategy for an organic rankine cycle waste heat recovery system. *Applied Energy*, 256:113991, 2019.
- Gary E Rochau. Supercritical co2 brayton cycle the DOE program. Technical report, Sandia National Lab.(SNL-NM), Albuquerque, NM (United States), 2011.
- G Scalabrin, P Marchi, F Finezzo, and R Span. A reference multiparameter thermal conductivity equation for carbon dioxide with an optimized functional form. *Journal of Physical and Chemical Reference Data*, 35(4):1549–1575, 2006.
- Roland Span and Wolfgang Wagner. A new equation of state for carbon dioxide covering the fluid region from the triple-point temperature to 1100 k at pressures up to 800 mpa. *Journal of physical and chemical reference data*, 25(6):1509–1596, 1996.
- Craig S Turchi, Zhiwen Ma, Ty W Neises, and Michael J Wagner. Thermodynamic study of advanced supercritical carbon dioxide power cycles for concentrating solar power systems. *Journal of Solar Energy Engineering*, 135(4):041007, 2013.
- HK Versteeg and W Malalasekera. *An introduction to computational fluid dynamics: the finite volume method*, chapter Solution algorithms for pressure-velocity coupling in steady flows. Prentice Hall, 2007.
- VGB PowerTech e.V. *Flexibility toolbox*. VGB PowerTech Service GmbH, Deilbachtal 173, 45257 Essen, Germany, 3 2017. ISBN 978-3-96284-046-4.
- Yasuhiro Wada and Meng-Sing Liou. An accurate and robust flux splitting scheme for shock and contact discontinuities. *SIAM Journal on Scientific Computing*, 18(3):633–657, 1997.
- Yang Wang and Stephen Boyd. Fast model predictive control using online optimization. *IEEE Transactions on control systems technology*, 18(2):267–278, 2010.
- F.M. White. *Fluid Mechanics*. McGraw-Hill series in mechanical engineering. McGraw Hill, 2011. ISBN 9780073529349.
- Arnold Whitfield and Nicholas C Baines. Design of radial turbomachines. Technical report, 1990.
- Adamu Yebi, Bin Xu, Xiaobing Liu, John Shutty, Paul Ansel, Zoran Filipi, Simona Onori, and Mark Hoffman. Estimation and predictive control of a parallel evaporator diesel engine waste heat recovery system. *IEEE Transactions on Control Systems Technology*, 27(1):282–295, 2017.